

Supplementary Materials for Ion beam subcellular tomography

Ahmet F. Coskun^{1,2,*}, Guojun Han^{1,*}, Shih-Yu Chen¹, Xavier Rovira Clavé¹, Sizun Jiang¹, Christian M. Schuerch¹, Yunhao Bai³, Chuck Hitzman⁴, and Garry P. Nolan¹

¹Baxter Laboratory, Department of Microbiology and Immunology, Stanford University School of Medicine, Stanford, CA

²Department of Radiology, Molecular Imaging Program at Stanford, Stanford University School of Medicine, Stanford, CA

³Department of Chemistry, Stanford University, Stanford, CA

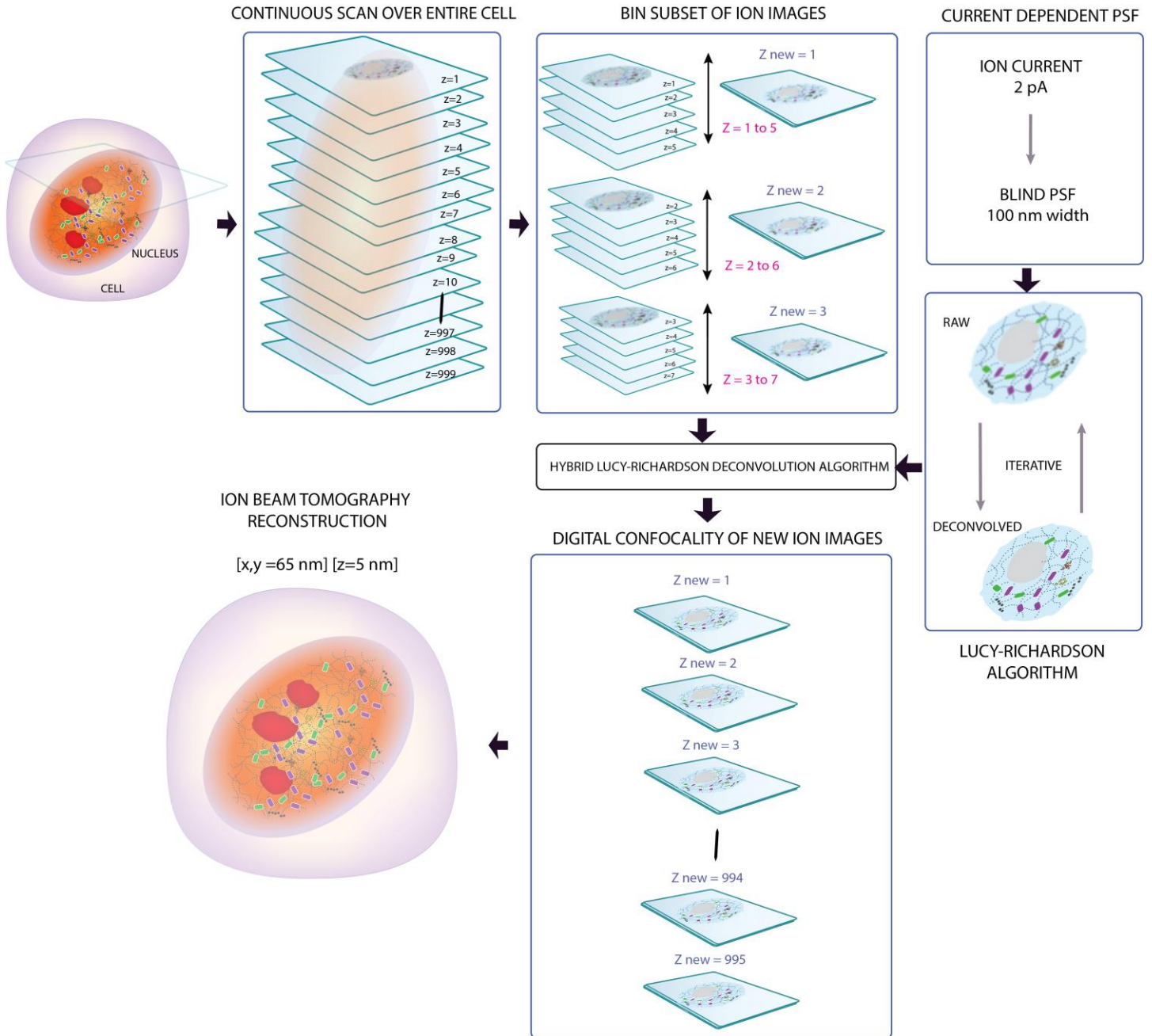
⁴Department of Materials Science and Engineering, Stanford University, Stanford, CA

*Co-first author

Supplementary File	Title
Supplementary Figure 1	Ion beam tomography pipeline
Supplementary Figure 2	Synthetic ion beam imaging and microscopy data
Supplementary Figure 3	Lateral resolution analysis of ion images captured by Cesium gun source for Au coated Si samples
Supplementary Figure 4	Lateral resolution analysis of ion images captured by Cesium gun source for Jurkat cell samples
Supplementary Figure 5	Resolution analysis of ion beam images captured by Oxygen gun source for Al coated Si samples
Supplementary Figure 6	Axial resolution analysis by a circular replication site
Supplementary Figure 7	Axial changes of sixty slices for subcellular region
Supplementary Figure 8	Axial resolution by cell height divided by total scans
Supplementary Figure 9	Modeling of ion beam imaging parameters
Supplementary Figure 10	Pixel size effect of ion beam acquisition on analysis
Supplementary Figure 11	Signal to noise ratio analysis on multi-slice sums
Supplementary Figure 12	Registration patterns for IBT
Supplementary Figure 13	Rapid depth etching by high current levels
Supplementary Figure 14	Schematic for depth imaging by IBT
Supplementary Figure 15	Elemental sensitivity analysis for Cesium and Oxygen
Supplementary Figure 16	Voxel and octree analysis of replication forks
Supplementary Figure 17	IBT results for chromatin images
Supplementary Figure 18	Structural similarity index values for DNA images
Supplementary Figure 19	Similarity of DNA images in another Nalm6 cell
Supplementary Figure 20	Fuzzy logic segmentation in a B cell lymphoblast
Supplementary Figure 21	Fuzzy logic segmentation in a HeLa cell
Supplementary Figure 22	Four channel replication experiment (2-hours)
Supplementary Figure 23	Repeat of replication dynamics experiment (30-min)
Supplementary Figure 24	Repeat of replication dynamics experiment (2-hours)
Supplementary Figure 25	Statistics of overlaps in replication experiments
Supplementary Figure 26	Newly synthesized transcript localization
Supplementary Figure 27	Replicate for transcription and replication in Nalm6
Supplementary Figure 28	Transcription and replication in a Nalm6 cell
Supplementary Figure 29	Long pulse (2-h) for transcription and replication
Supplementary Figure 30	Transcription inhibitors during 2-h metabolic labeling
Supplementary Figure 31	Transcription signal reduction by α -amanitin
Supplementary Figure 32	Transcription and replication (color swap) in Nalm6
Supplementary Figure 33	3D mature transcription in HeLa by RNA FISH labeling
Supplementary Figure 34	Mature and nascent transcription in Jurkat and Nalm6

Supplementary Figure 35	Label-free mass imaging in FFPE tissues
Supplementary Figure 36	Volumetric histology by IBT
Supplementary Methods	

Computational pipeline for Ion beam subcellular tomography



Supplementary Figure 1. IBT mathematical pipeline.

Ion images are acquired across 1,000 depth sections.

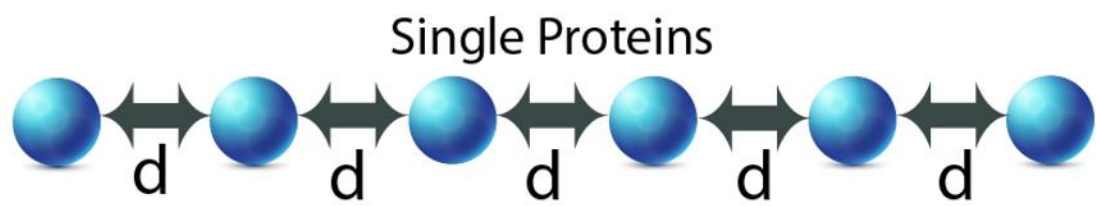
A subset of raw ion scans is binned (in this example, over five slices) to generate a new ion image with high signal to noise ratio (SNR) and less noise. This process is incremented by one slice at a time, providing a new ion image series with a similar dimension. The last few slices are skipped due to windowing.

A current-dependent point spread function is calculated for the deconvolution process.

Each ion image is then deblurred by an iterative Lucy Richardson deconvolution algorithm.

Five iterations were optimum for typical ion images but must be optimized based on SNR of the images.

The resultant sharper ion images are then stitched over axial direction for error-free reconstructions.

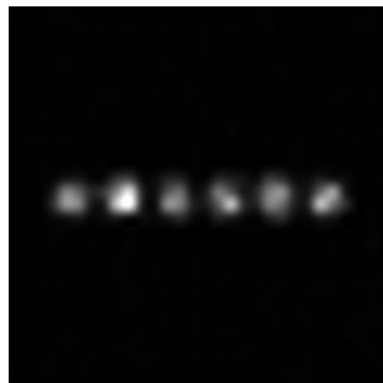
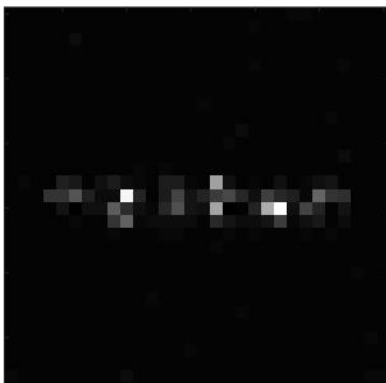
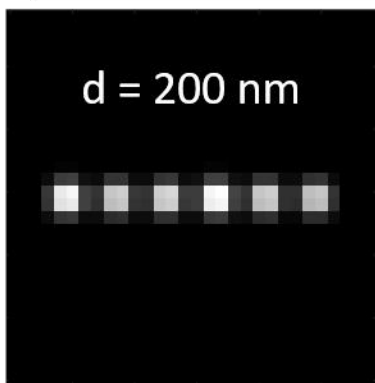


Raw Image

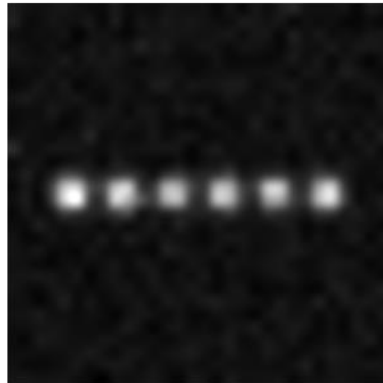
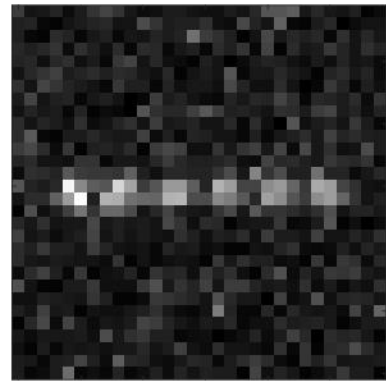
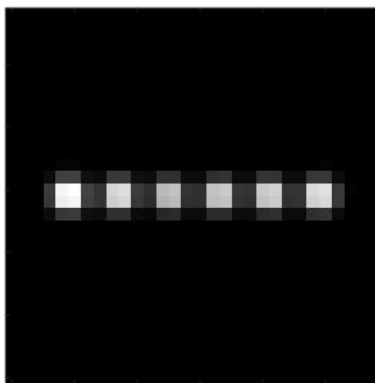
Raw Image w/ Noise

Reconstruction

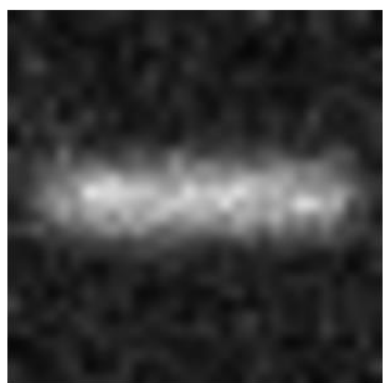
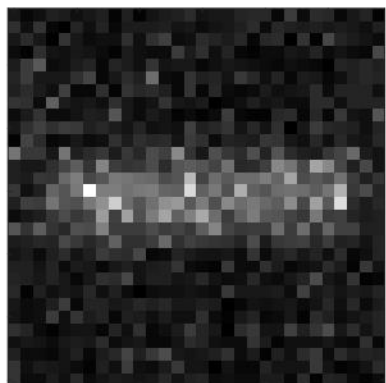
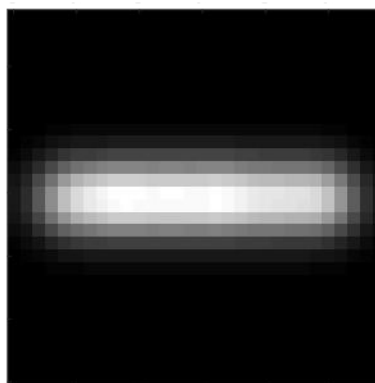
Ion Beam
Imaging



Super Resolution
Fluorescence



Confocal
Fluorescence



Supplementary Figure 2. A simulated array used to evaluate the ion beam analysis pipeline.

Six protein signatures with a separation of 200 nm were generated for

Ion beam imaging (PSF: 120 nm; pixel size: 50 nm)

Super-resolution fluorescence imaging (PSF: 50 nm; pixel size: 50 nm)

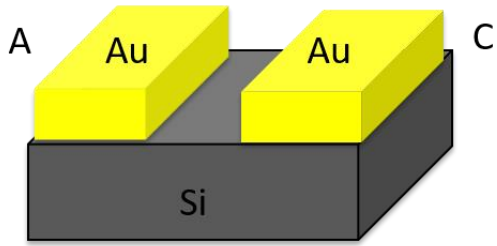
Confocal fluorescence microscopy (PSF: 250 nm; pixel size: 100 nm).

Super resolution was assumed to be a STORM imaging platform for a computational PSF of 50 nm after reconstructions (real PSF size and localization process are not detailed here).

Noise was then measured from experimental images and used to contaminate each synthetic image.

Ion beam images have higher noise variation than fluorescence images.

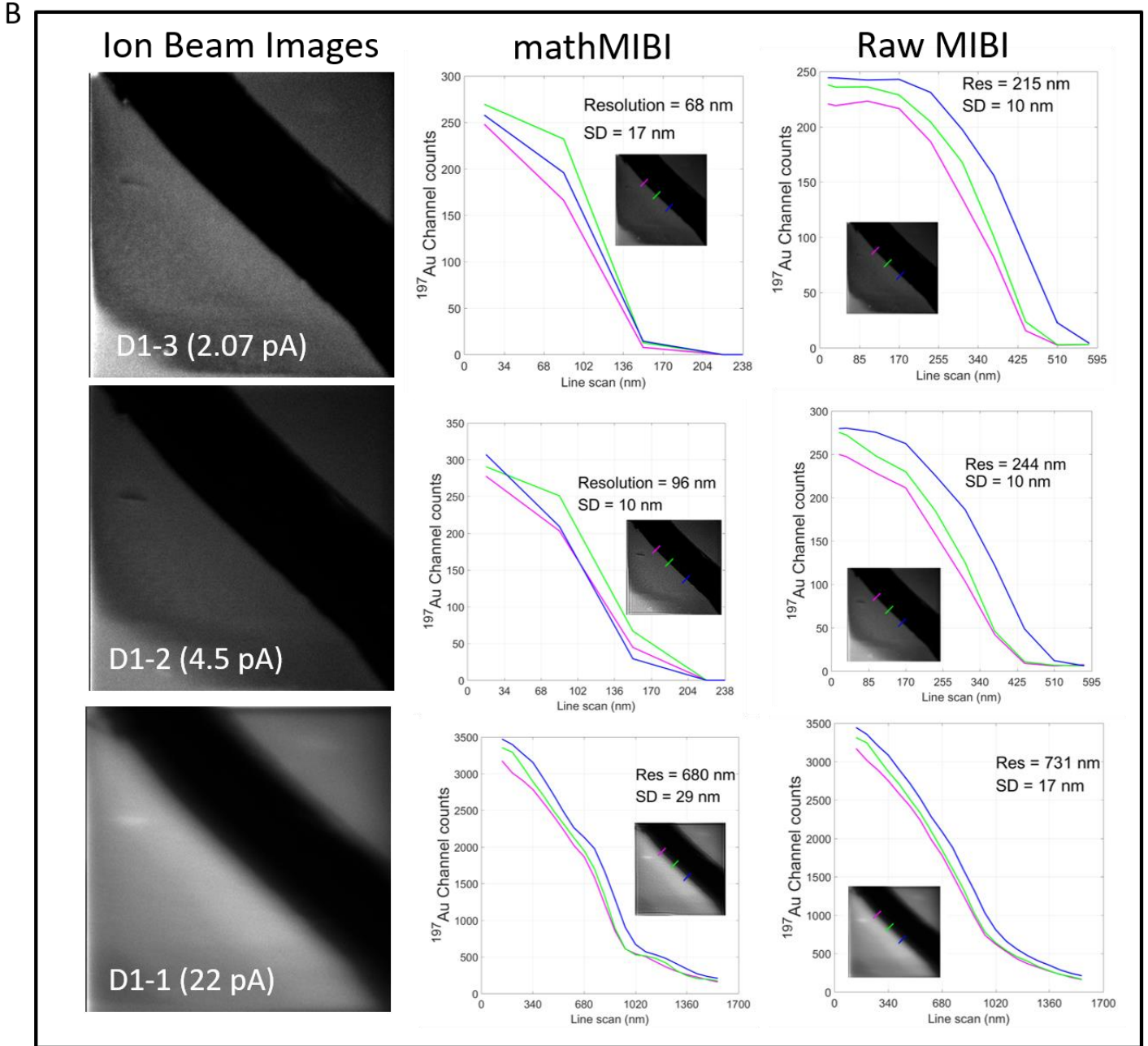
The IBT mathematical pipeline was then validated after reconstruction of the noisy ion beam and fluorescence images.



C

	D1_1		D1_2		D1_3	
	Math	Raw	Math	Raw	Math	Raw
Set	689	731	96	244	68 nm	215

Set



Supplementary Figure 3. IBT mathematical framework results in down to 68-nm lateral resolution.

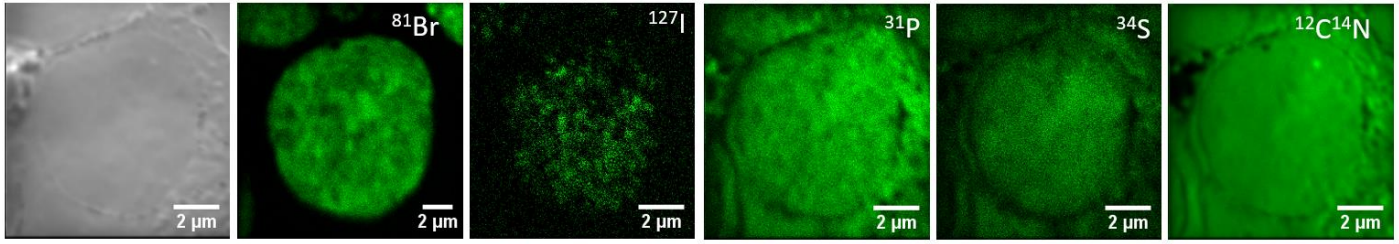
(a) Au-coated silicon substrates were used to quantify spatial resolution in ion beam images generated by a cesium source.

(b) Ion beam images were acquired at 2.07, 4.5, and 22 pA using D1-3, D1-2, and D1-1 apertures, respectively. Three cross-sections at the edge of Au-Si were used to quantify spatial resolution. Insets show processed ion images with blue, green, and magenta line plots for 2.07, 4.5, and 22 pA, respectively.

(c) Summary of resolution limits of raw MIBI and reconstructed IBT images by mathematical analysis of MIBI (mathMIBI).

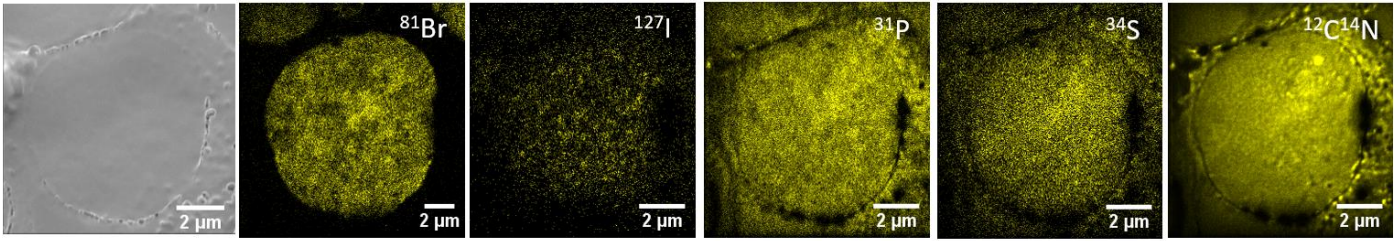
A

Ion Beam with D1-3 (4 pA)

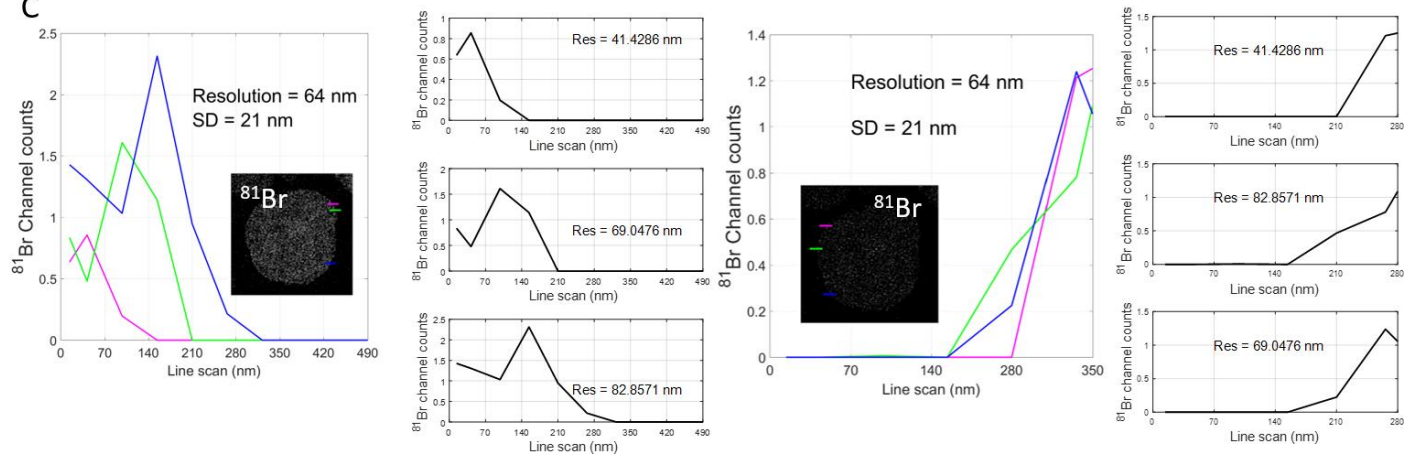


B

Ion Beam with D1-3 (0.155 pA)



C

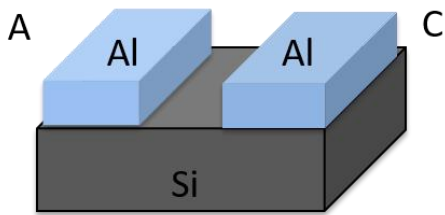


Supplementary Figure 4. Six-color ion beam imaging experiment for endogenous elements (^{12}C , ^{14}N , ^{34}S : total proteins; ^{31}P : DNA backbone) and metabolite labels and replication loci (labeled with ^{127}I -dU for 24 hours and ^{81}Br -dU for 30 minutes) in Jurkat cells.

(a) Seven channel ion beam images of a Jurkat cell by D1_3 setting corresponding to 4 pA of ion current.

(b) Same cell was imaged at 0.155 pA current, highest resolution setting with smallest feasible ion beam width.

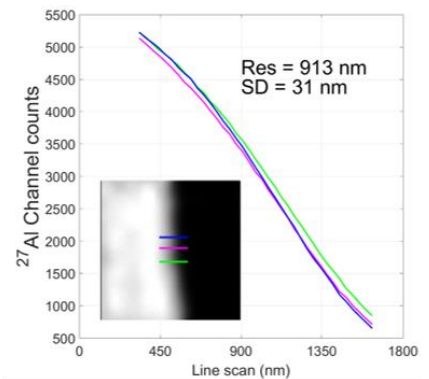
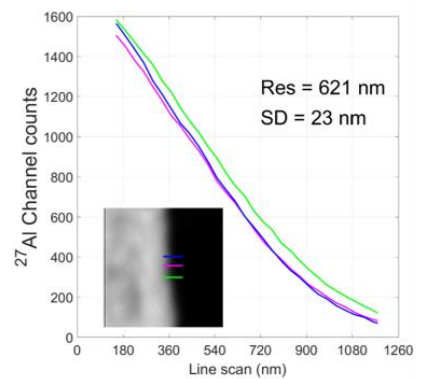
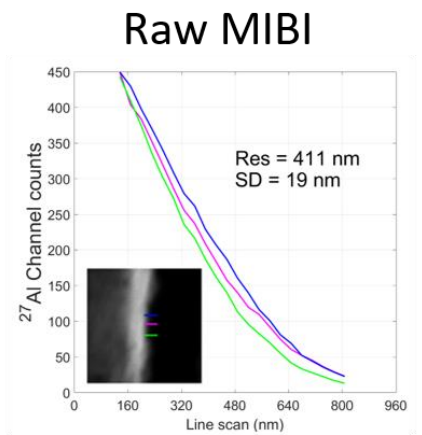
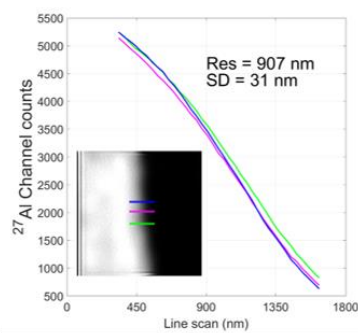
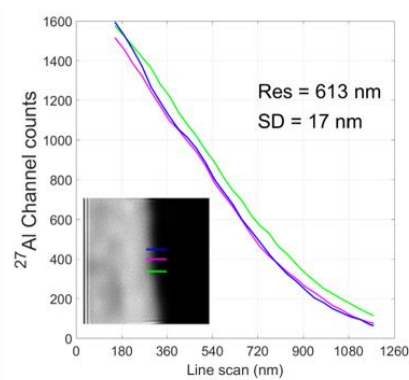
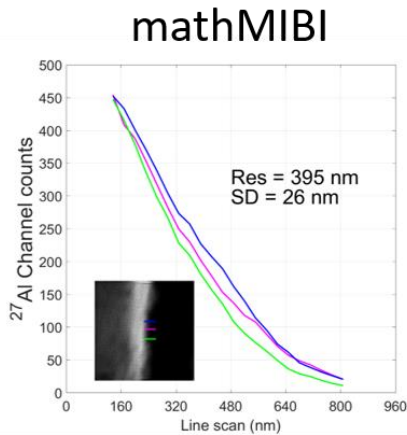
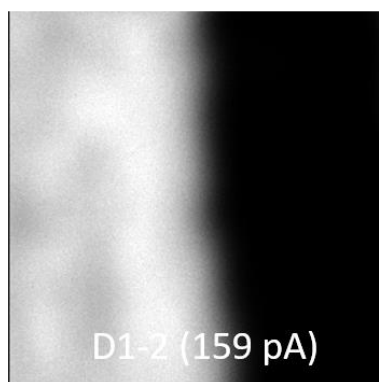
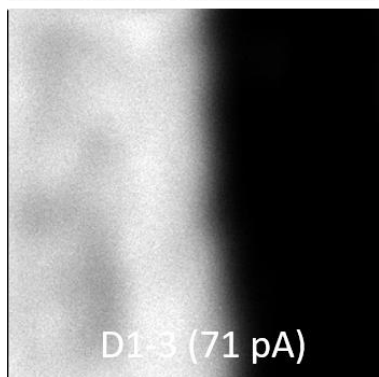
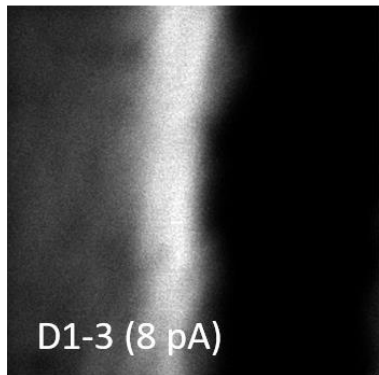
(c) Three distinct line scans were measured across right and left edges of the image detected at the ^{81}Br channel. Blue, red and magenta colors correspond to the line scan positions on the cell image and cross section plots. In both edges, the distance through which the ^{81}Br ion signal drops to 16% of the maximum yielded $65\text{ nm} \pm 21\text{ nm}$ (STD) spatial resolution, agreeing well with the gold edge on silicon substrate experiment shown in Supplementary Fig. 3.



C

	D1_2-159pA		D1_3-71pA		D1_3-8pA	
	Math	Raw	Math	Raw	Math	Raw
Set	907	913	613	621	395 nm	411

B Ion Beam Images



Supplementary Figure 5. Resolution characterization for ion images acquired using an oxygen source using deconvolution and analysis parameters similar to those described in Supplementary Fig. 2.

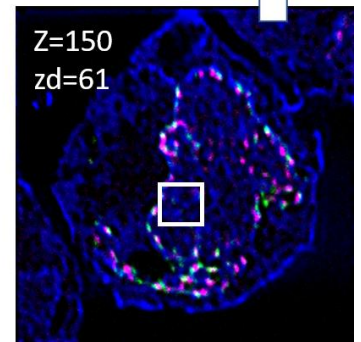
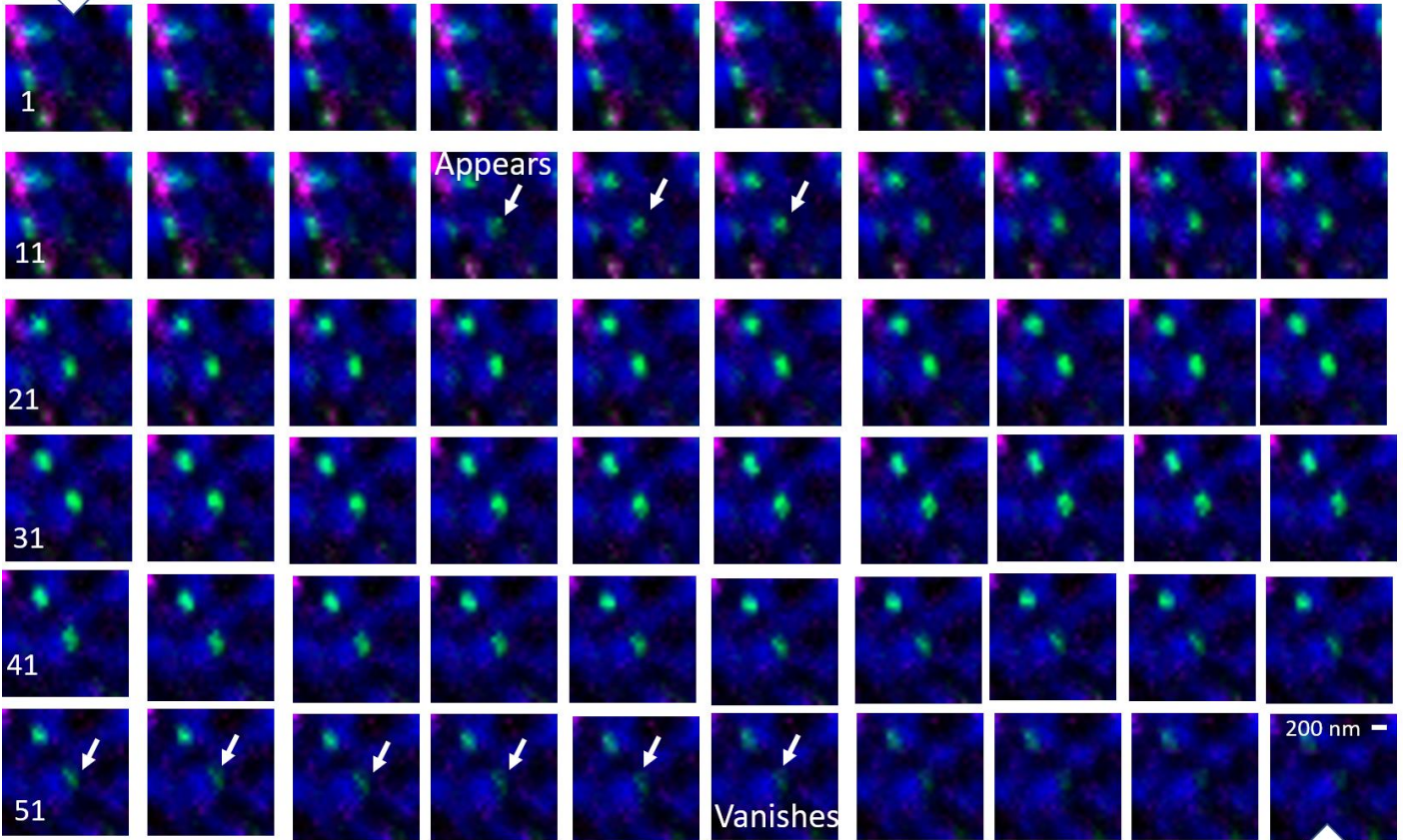
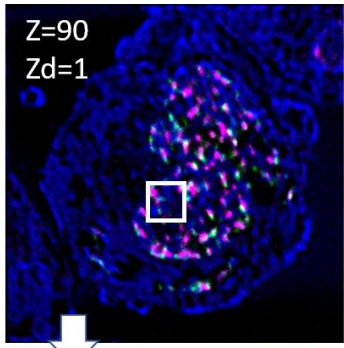
(a) An Al-coated silicon substrate was used to measure the edge profile.

(b) Ion beam images were acquired at 8, 71, and 159 pA using D1-3, D1-2, and D1-1 apertures, respectively. Three cross-sections at the edge of Al-Si were used to quantify spatial resolution. Insets show processed ion images with blue, green, and magenta line plots for 8, 71, and 159 pA, respectively.

(c) Summary of resolution limits of raw MIBI and reconstructed IBT images by mathematical analysis of MIBI data (mathMIBI).

Spatial resolution levels down to 395 nm were achieved. Larger iteration numbers will reduce these resolution levels while image artifacts may increase as a result of the processing. Due to the large beam width, computation faces challenges to decouple overlapping ion signals in the digital processing. Had the edge of this test substrate been sharper more stringent resolution criteria could have been obtained. Oxygen beam experiments are not the focus of this paper, but the IBT algorithm works on these images with decent resolution enhancements. Sub-500 nm resolution levels are sufficient for study of tumor samples obtained from biopsies.

Axial resolution determination by a single replication fork



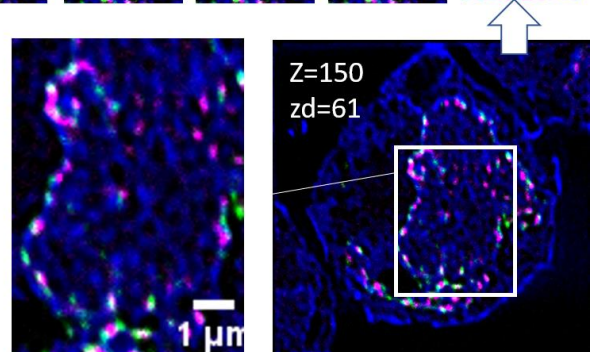
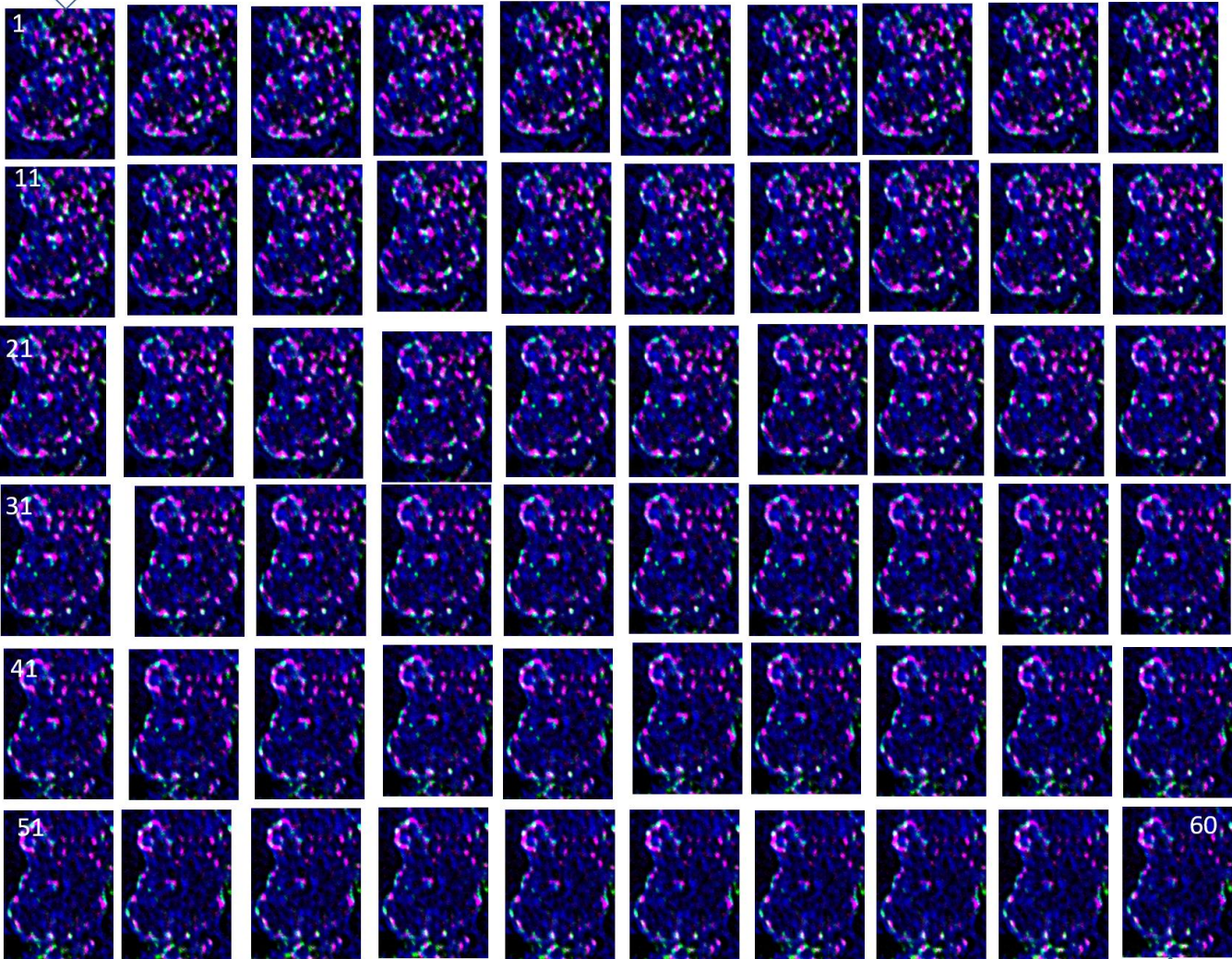
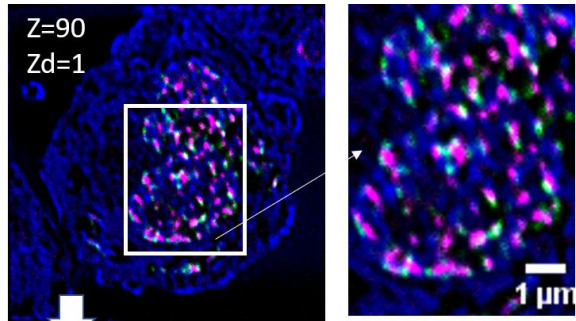
Supplementary Figure 6. Estimation of axial resolution by replication fork imaging.

^{31}P channel (largely chromatin, referred as DNA) in blue, ^{127}I -dU was a replication site in green, and ^{81}Br -dU was another replication site in magenta. Each replication was a result of 30 minutes incorporation.

Sixty slices of two replication forks in ^{127}I -dU channel reveal a 3-pixel replication site (size=175 nm in one direction) appearing around the 15th slice and vanishing around 55th slice.

From this image, the axial resolution was estimated to be approximately 5 nm as the 175-nm replication site extends over 40 slices.

High resolution depth imaging of replication forks by ion beam tomography

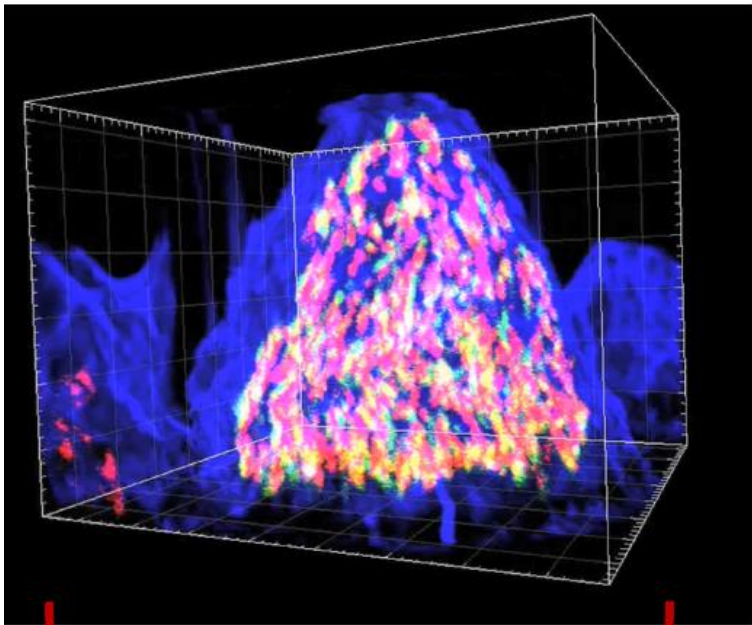


Supplementary Figure 7. Estimation of axial resolution by imaging of a single cell.

Similar to the previous figure: ^{31}P channel (blue), ^{127}I -dU (green), and ^{81}Br -dU (magenta).

Sixty consecutive depth images of a Nalm6 cell shows slight differences at every scan with 5-nm slice thickness indicative of approximately 5-nm axial resolution for IBT.

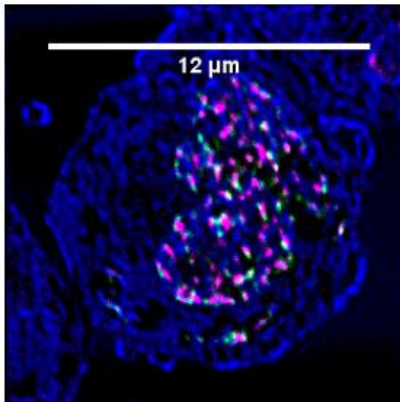
Tomographic thickness of a cell for axial resolution analysis



Z dimension (<math><10\mu\text{m}</math>)

1,000
MIBI
slices

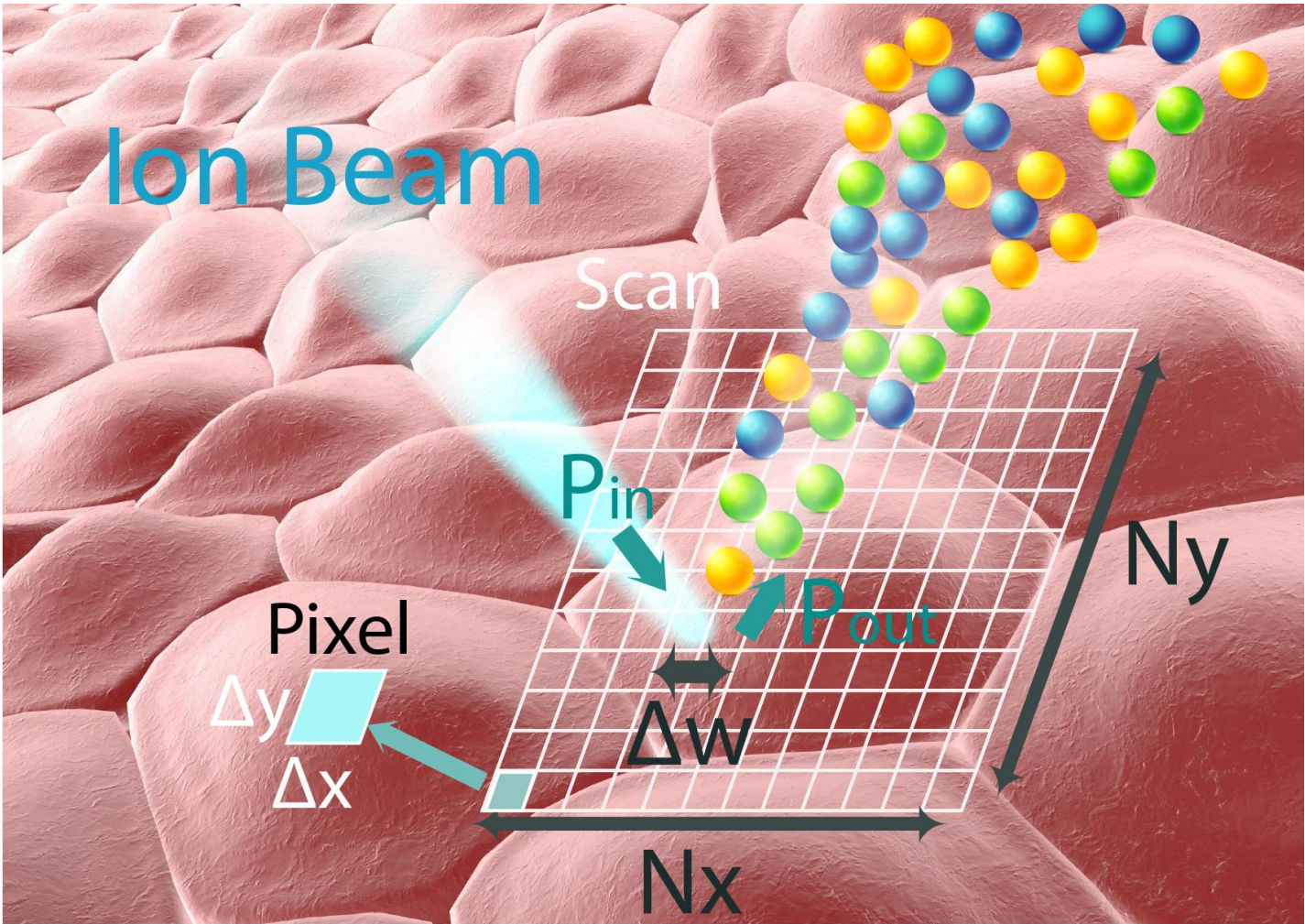
X-Y dimensions



Supplementary Figure 8. Estimation of axial resolution by imaging of a single cell.

One thousand scans were etched through a Nalm6 cell. The lateral extent of the cell is between 10 and 12 μm .

Due to the dehydration process and spin coating of cells during preparation, the axial extent is between 5 and 10 μm , yielding an estimate of 5-10 nm axial resolution.



Supplementary Figure 9. Modeling of ion beam imaging parameters.

Ion beam source (blue) corresponds to either Cesium or Oxygen source, impinging on the sample of interest.

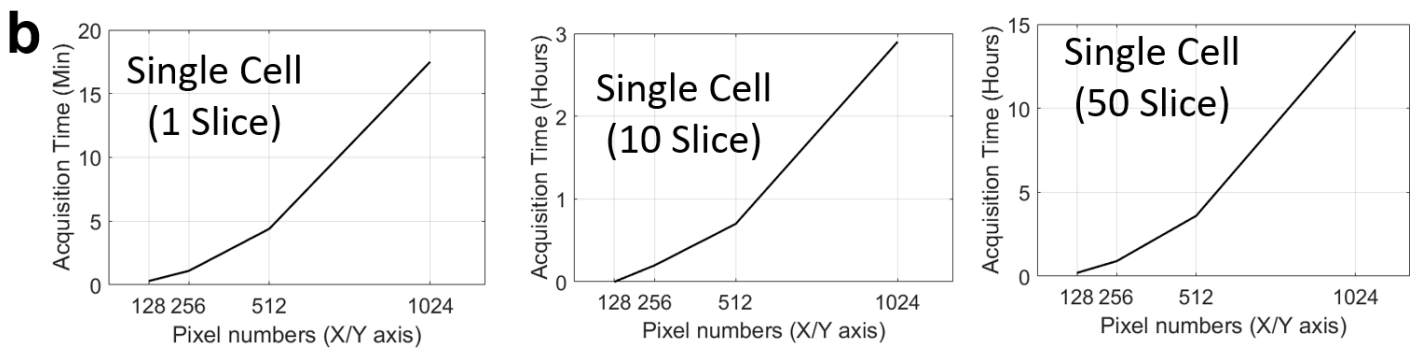
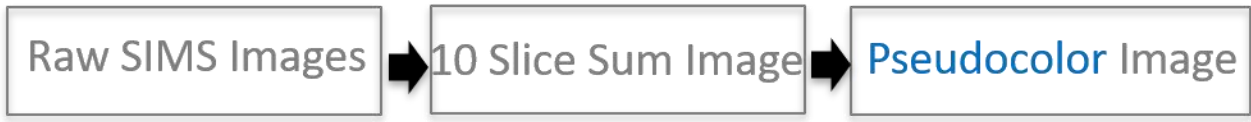
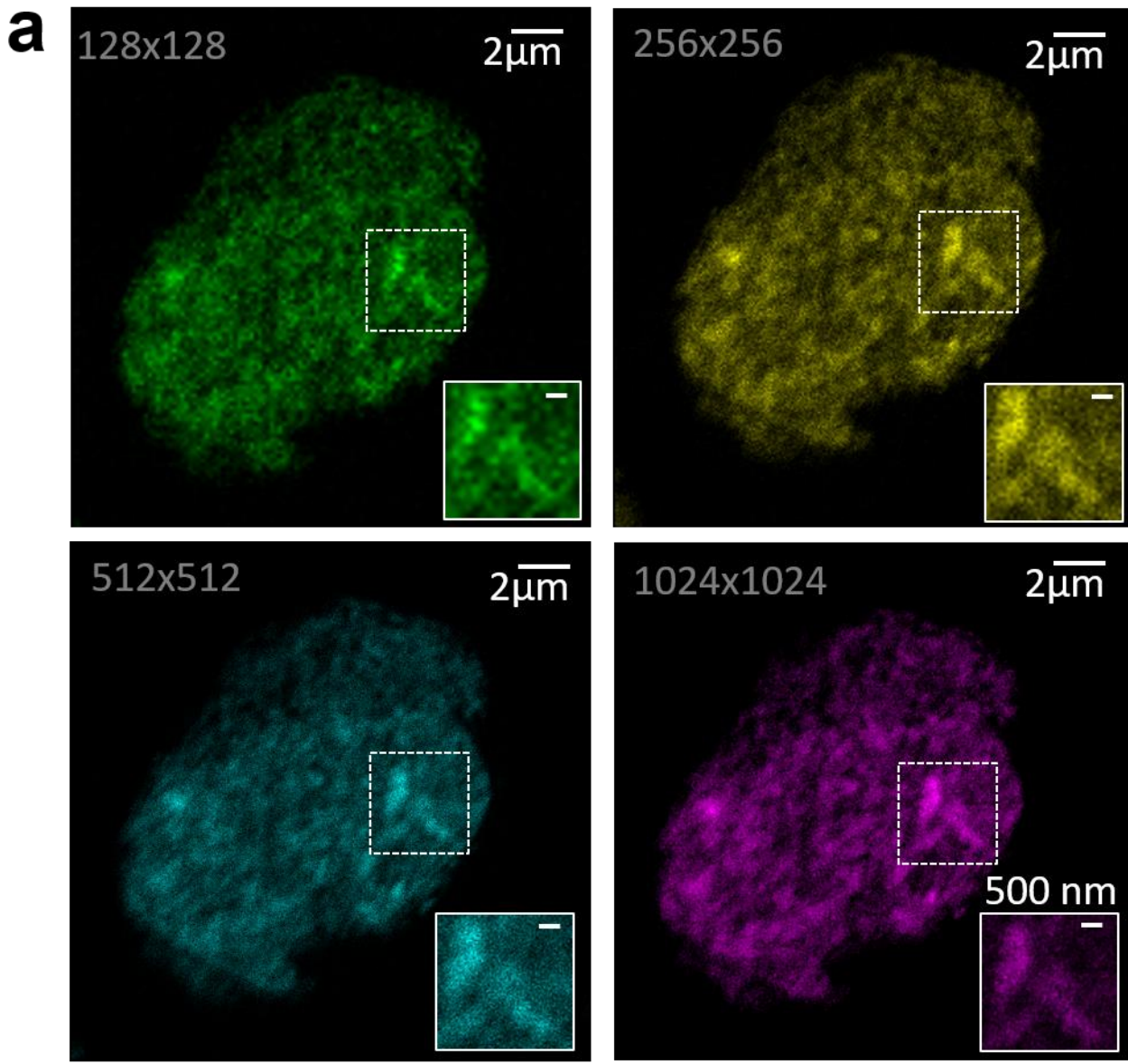
After focusing down to sub-100 nm, incoming ion signal (P_{in}) to the sample within a small subcellular voxel.

Total secondary ions extracted from the sample (P_{out}) and was calculated to be 3%. Distinct color (round objects) correspond to different mass labels.

Pixel size dimensions Δx and Δy of these ion beam images: In the range of 50-150 nm in both dimensions.

Total number of pixels per axis, $N_x \times N_y$ pixels, typically 256x 256 pixels, 512x 512 pixels.

Ion beam width of Δw that is determined by the ion beam optics and aperture settings: 50-500 nm wide.



Supplementary Figure 10. Pixel size effect for ion beam imaging.

(a) HeLa cell DNA imaged by ^{127}I channel after 24-hour incubation with ^{127}I -dU to label DNA.

Four different scans with unique pixel size values were captured for the same cell.

A 25- μm window was imaged and divided into 128 x 128 pixels, 256 x 256 pixels, 512 x 512 pixels, or 1024 x 1024 pixels.

Dividing the imaging window by the number of pixels yielded 156 nm, 78 nm, 39 nm, and 19 nm pixel sizes, respectively.

Ten consecutive frames were then summed and pseudocolored in MATLAB. These images were captured with 100-nm PSF width. Imaging pixel size must be smaller than 100 nm to record details of interest.

Thus, the 156-nm pixel size image was not able to resolve details whereas 78-, 39-, and 19-nm pixel sizes provided similar quality images. Sub-50-nm pixel size exposes the same area to ion beams multiple times, creating an oversampling effect in the images.

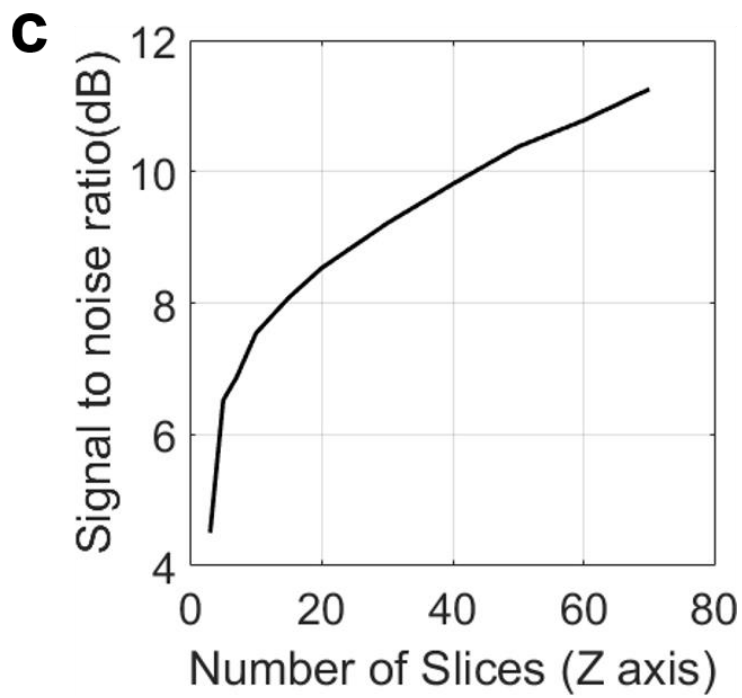
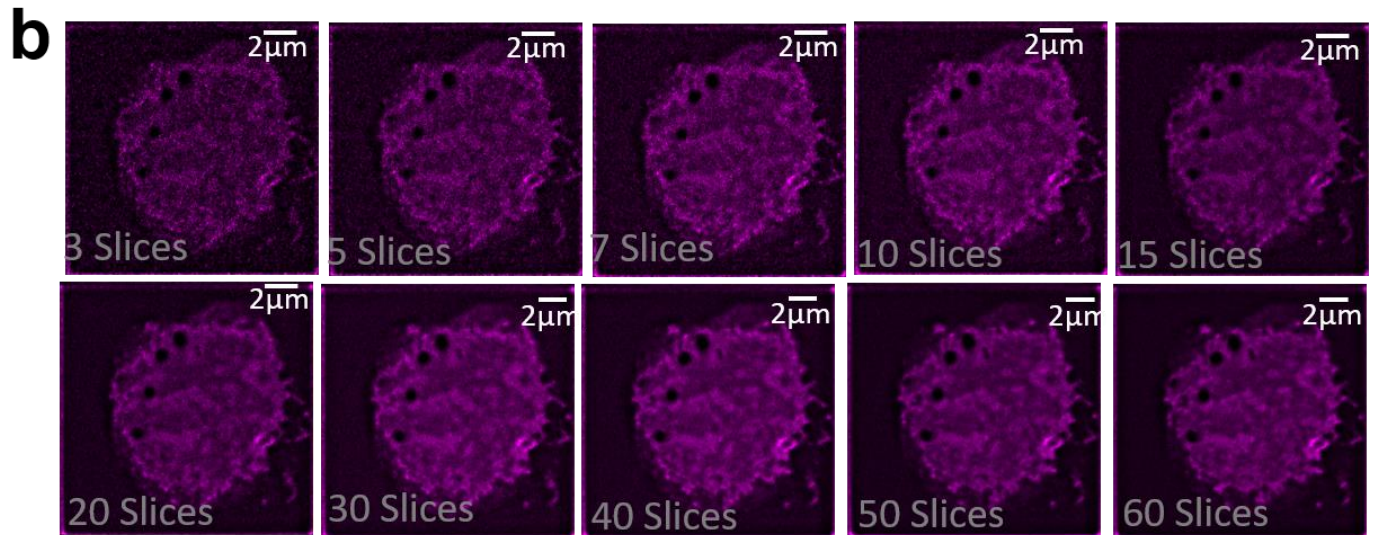
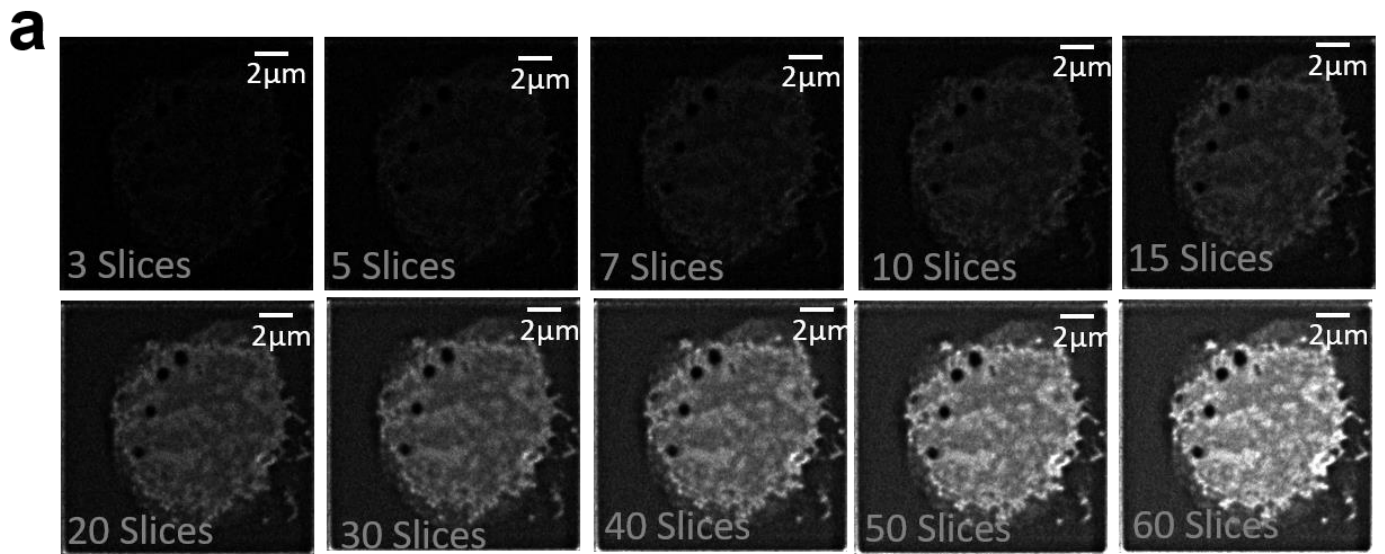
(b) Image acquisition time scales with numbers of pixels and slices:

Single slice takes more than 15 minutes at 1024x1024 sampling.

Ten slices require up to 3 hours for the same pixel size.

Fifty slices consume about 15 hours with the same pixel dimensions.

A window size of 256 x 256 pixels is the optimal for acquisition time, sampling accuracy, and spatial resolving capability.



Supplementary Figure 11. Multiple depth binning enhances signal-to-noise ratio.

(a) Seventy sections from the same K562 cell were analyzed. The signal-to-noise ratio (SNR) was enhanced as slices were added.

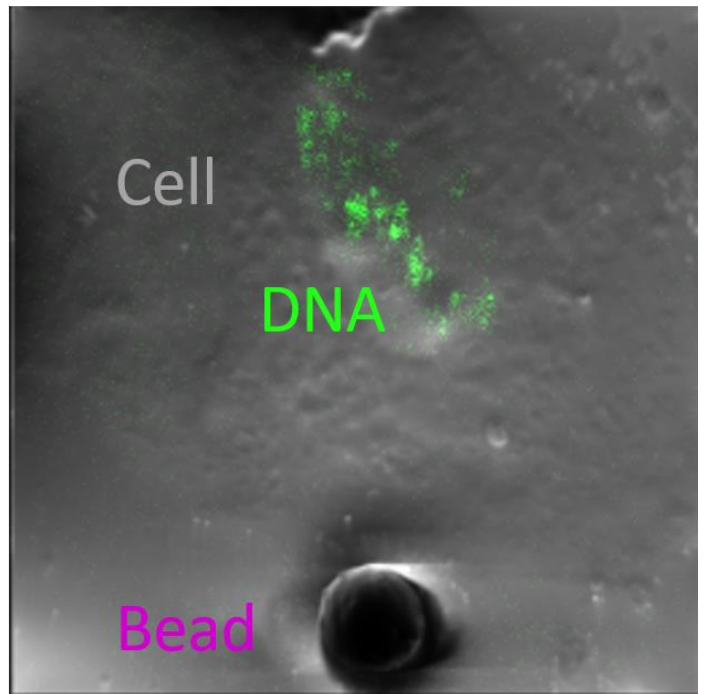
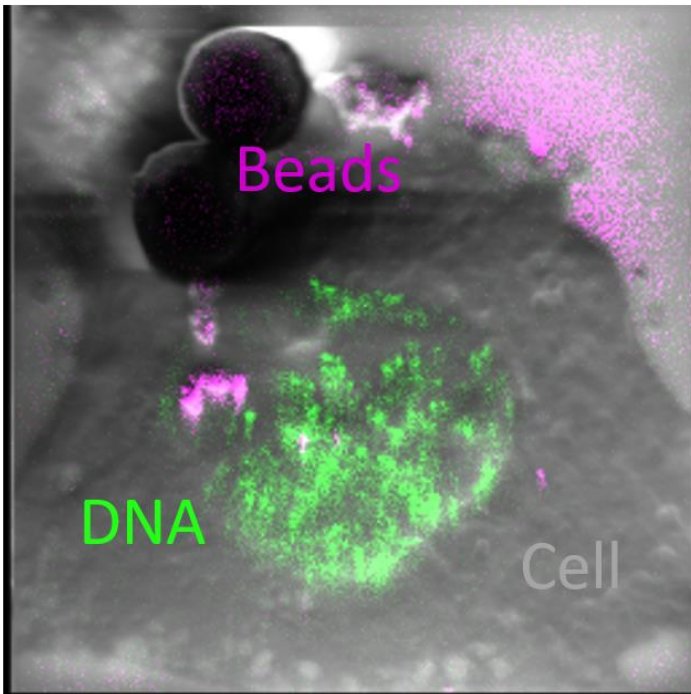
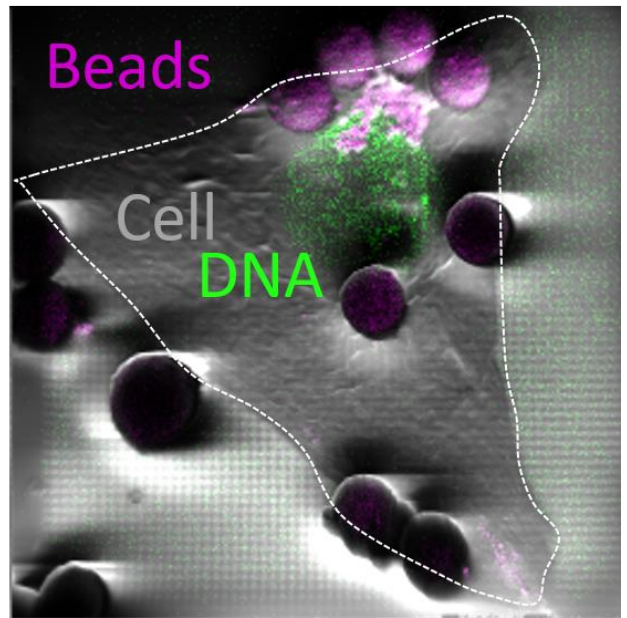
(b) Separately adjusted contrast levels of ion beam images demonstrated optimal spatial details with 10 to 20 slices summed.

(c) The plot of SNR versus number of slices summed indicates that there was exponential enhancement up to 15 slice sums, after which the SNR enhancement provided less improvement.

Ion bombardment



Beads
Fiducial markers

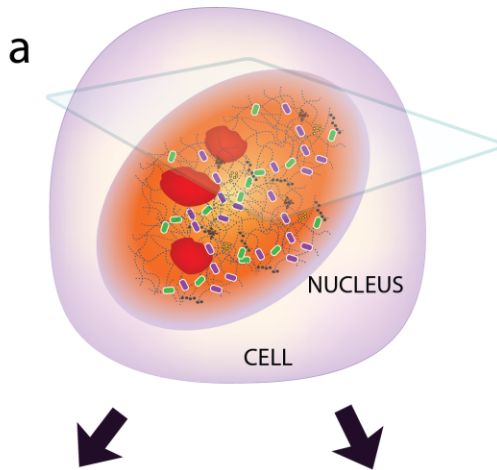


Supplementary Figure 12. Microbead addition enables correction for spatial offsets for each depth image. Beads can be used either outside the cell or inside the cell.

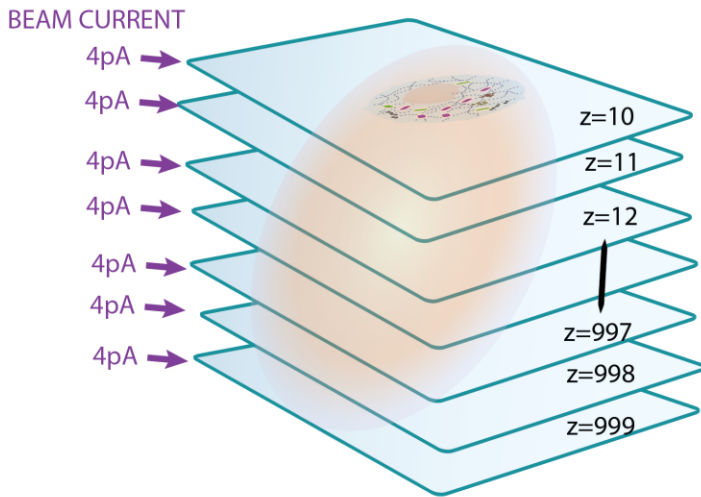
As the bead is made up of harder material than cellular contents, the etching of the bead requires a longer time than the etching of the cellular material. As a result of the differences in etch rates, the bead pattern looks similar across different scans.

The edge or the center of the bead is then used to correct the lateral shifts.

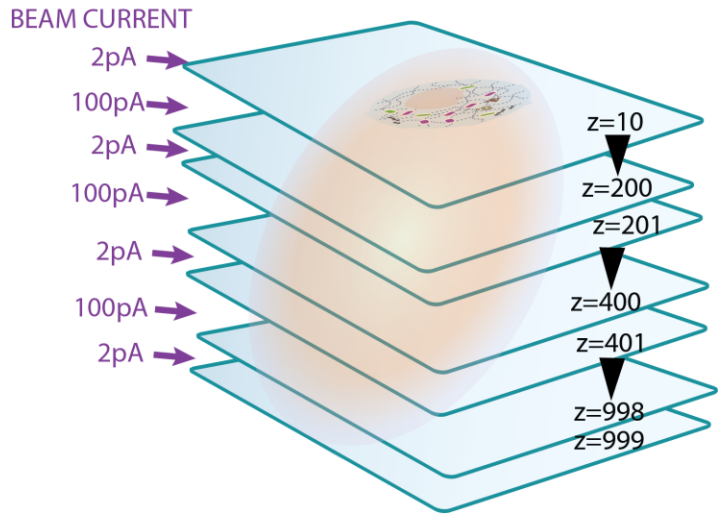
To reduce coagulation, beads are washed with water and ethanol prior to the experiments. The bead solution is then loaded onto the silicon substrate and spin coated at 125 RCF for 5 minutes.



b CONTINUOUS SCAN OVER ENTIRE CELL
(Higher current & small imaging area)



c CHAIN MODE
(High current + small current mix)



Supplementary Figure 13. Alternative imaging modes are available.

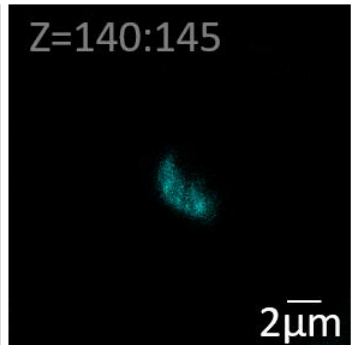
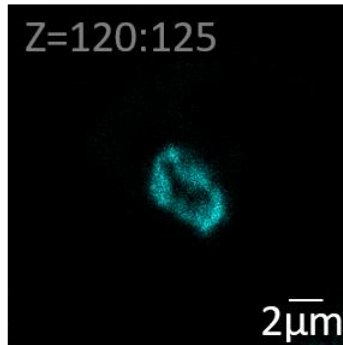
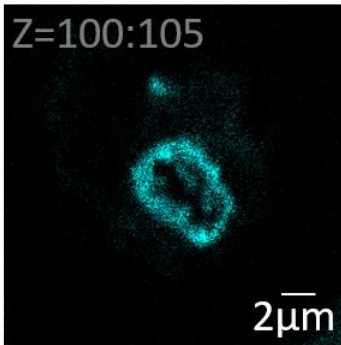
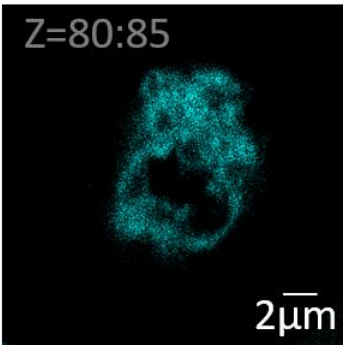
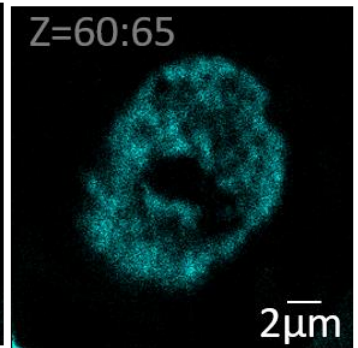
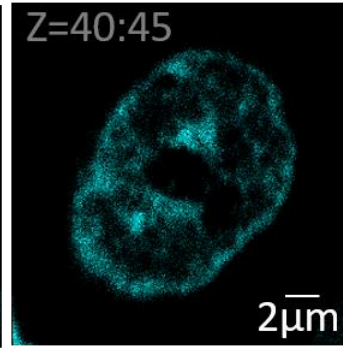
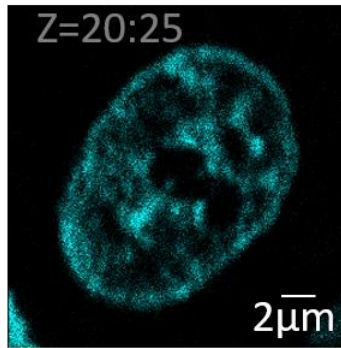
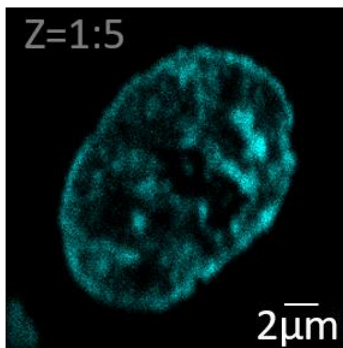
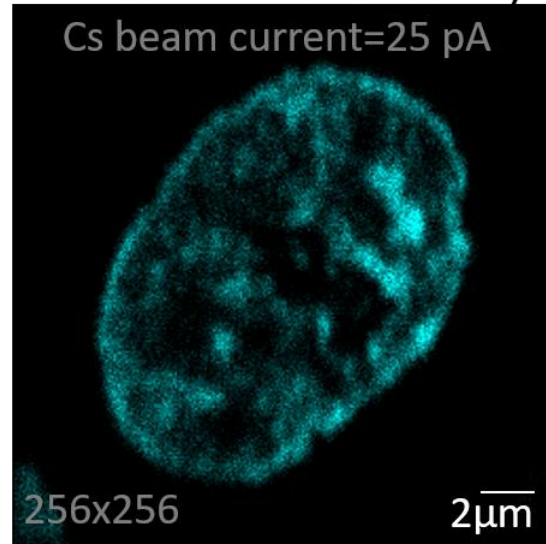
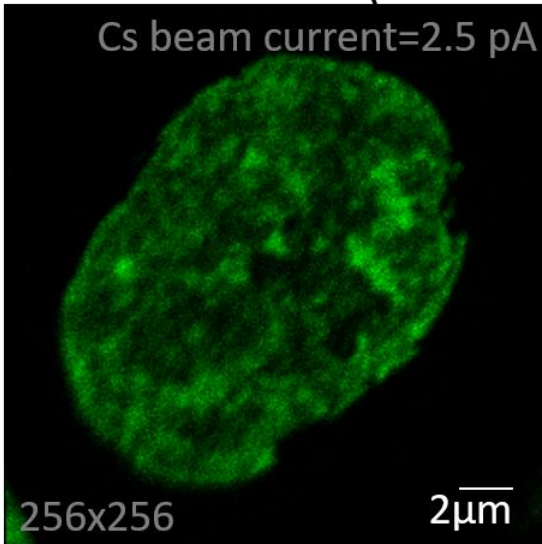
(a) A single cell is imaged from top to bottom by ion beam tomography.

(b) 3D image acquisition by continuous scans using low current (in the range of 0.2 to 4 pA) only for high resolution mapping of the entire cellular volume.

(c) Another ion imaging modality is chained mode.

Depth scans were acquired by a mix of high current (100pA) and low current (e.g., 2 pA), enhancing overall IBT throughput.

HeLa Cells (IdU Labeled DNA at ^{127}I Channel)

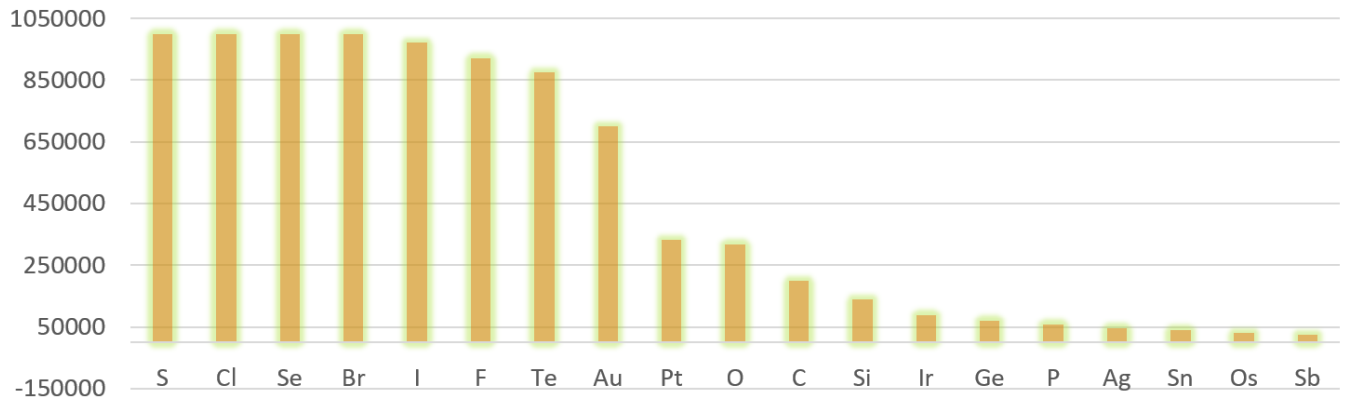
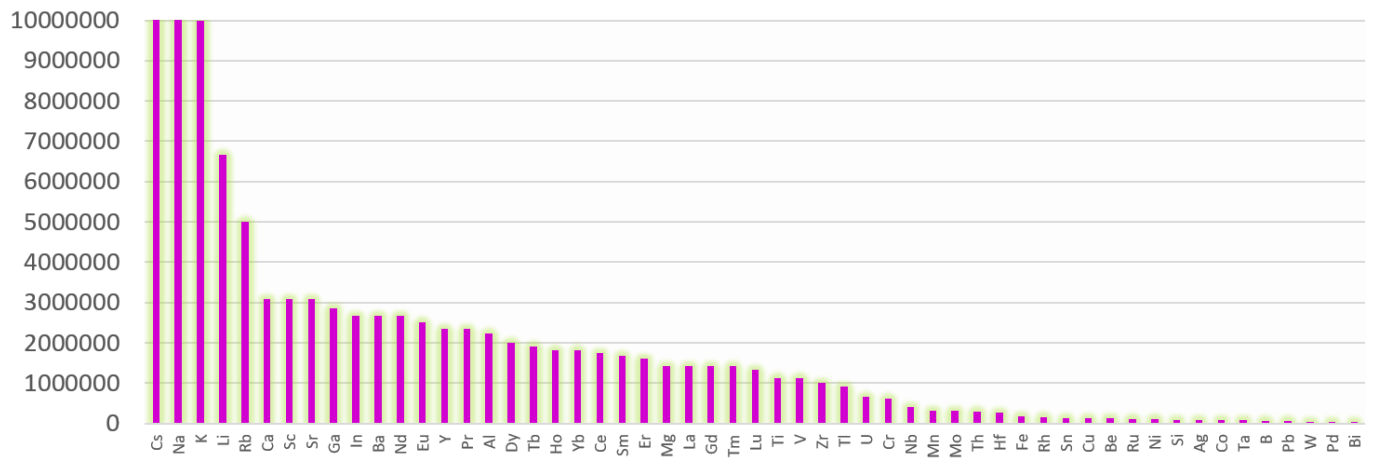


Supplementary Figure 14. Rapid depth imaging at decent spatial resolution.

HeLa cell was labeled with ^{127}I -dU for tagging DNA to be imaged by ion beams.

A higher current level (25 pA) was used to acquire the cell across 150 slices, rather than capturing up to 1,000 at 2.5 pA.

This approach reduced imaging time per cell, allowing to scan more cell in shorter duration.

A**Elemental sensitivity (Cesium source)****B****Elemental sensitivity (Oxygen source)**

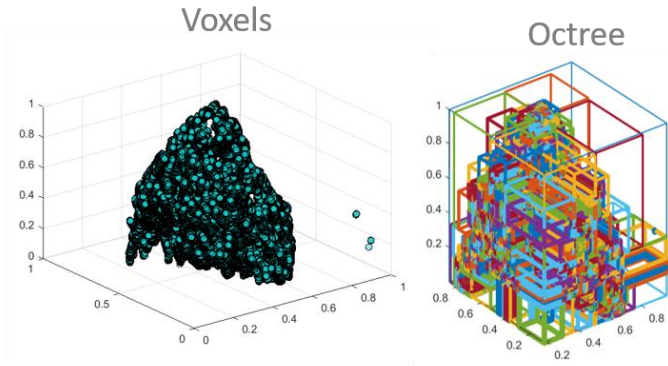
Supplementary Figure 15. Elemental sensitivity analysis of ion images acquired using cesium and oxygen sources.

The raw values were extracted from a previous publication (*Wilson. SIMS quantification in Si, GaAs, and diamond – an update. International Journal of Mass spectroscopy and Ion Processes, 143, 43-49, 1995; Table 1*).

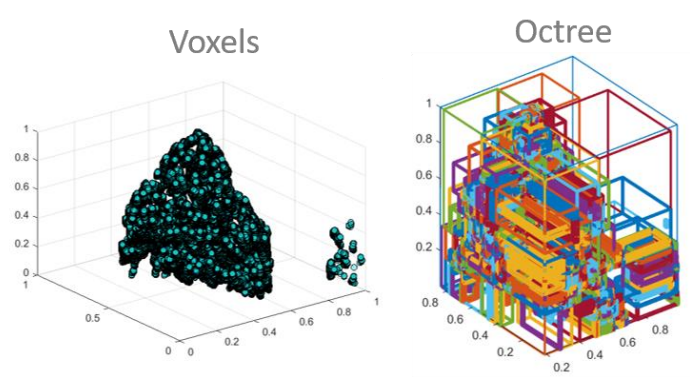
For the cesium source-based ion beam imaging, the relative sensitivity factors (RSF) of E^- RSF^b (Negative secondary ions measured by 14.5 keV Cs⁺ source) were divided by the max value of the RSF (lowest sensitivity number), providing a direct measure of sensitivity.

For the oxygen source, E^+ RSF^a (Positive secondary ions measured by 4 keV O⁺ source) values were also normalized by the largest number to enable sensitivity comparisons.

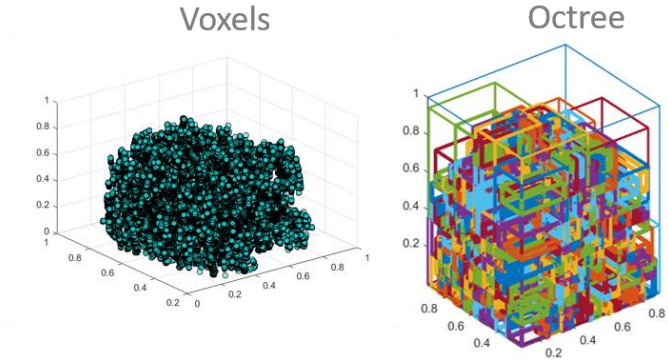
A ^{127}IdU (30-min chase)



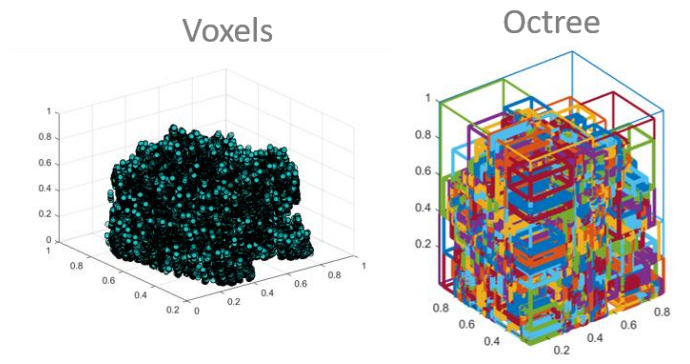
B $^{81}\text{BrdU}$ (30-min chase)



C ^{127}IdU (2-h chase)



D $^{81}\text{BrdU}$ (2-h chase)



Supplementary Figure 16. Voxel distributions and octree representations of replication forks in Nalm6 cells. Ion beam signal distribution in a single cell volume was partitioned into the eight octant subvolumes as part of the octree algorithm. The boxes show the density of ion signal within that particular volumetric space.

(a) Left corresponds to the cell that was pulsed with ^{127}I -dU incorporation for 30 minutes, and

(b) the right image shows another 30 minutes pulse with ^{81}Br -dU, that were chased 30 minutes in between the pulses in the culture. Octree distributions in these upper panels showed similar box patterns.

Similarly,

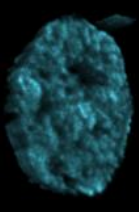
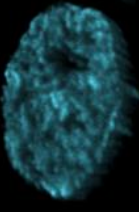
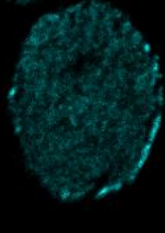
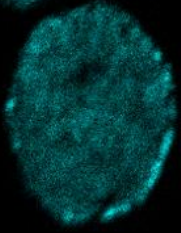
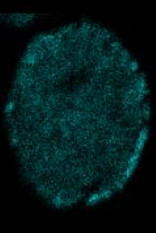
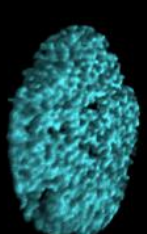
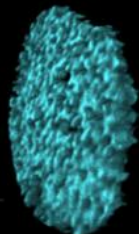
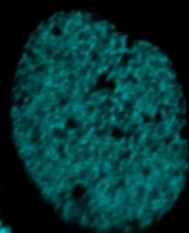
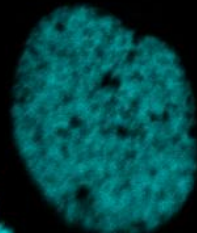
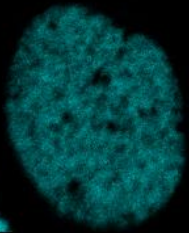
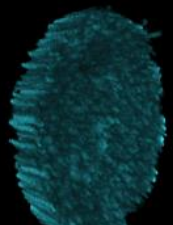
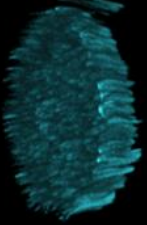
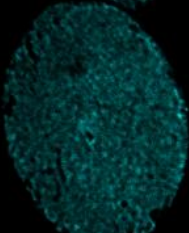
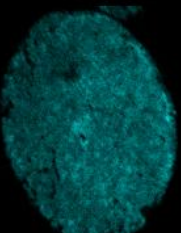
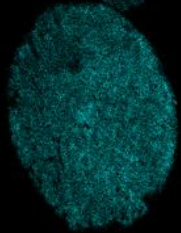
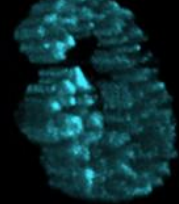
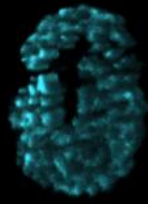
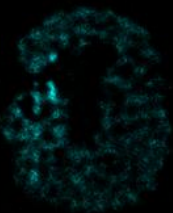
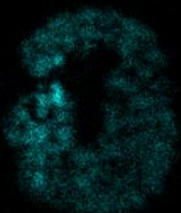
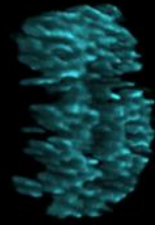
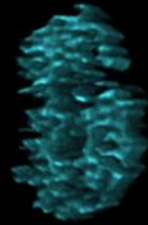
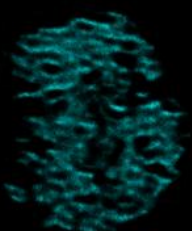
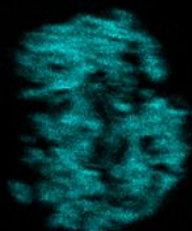
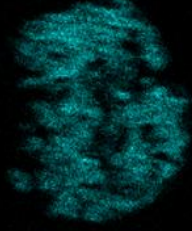
(c) lower left demonstrates I-dU and (d) right shows Br-dU incorporation separated with 2 hours chase time. Octree method yielded repeatable box patterns in the single cell volume.

Raw

Sum

Confocal

3D Renders



Supplementary Figure 17. IBT approach was validated in genomic images by ^{127}I channel using 24 hours of ^{127}I -dU labeling in Jurkat cells (top 2 rows) and HeLa cells (bottom 3 rows).

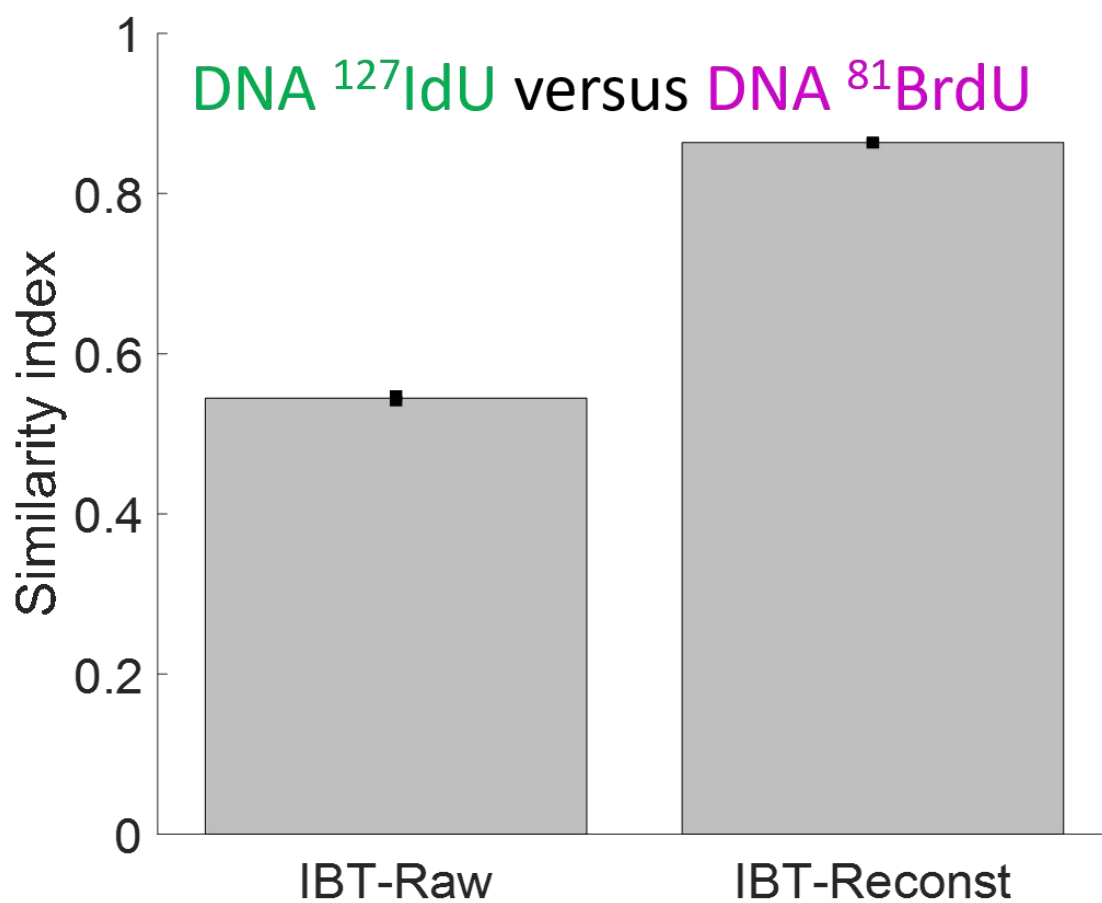
Raw: Acquired ion beam at each depth scan.

Sum: Binning of 5 subsequent depth slices.

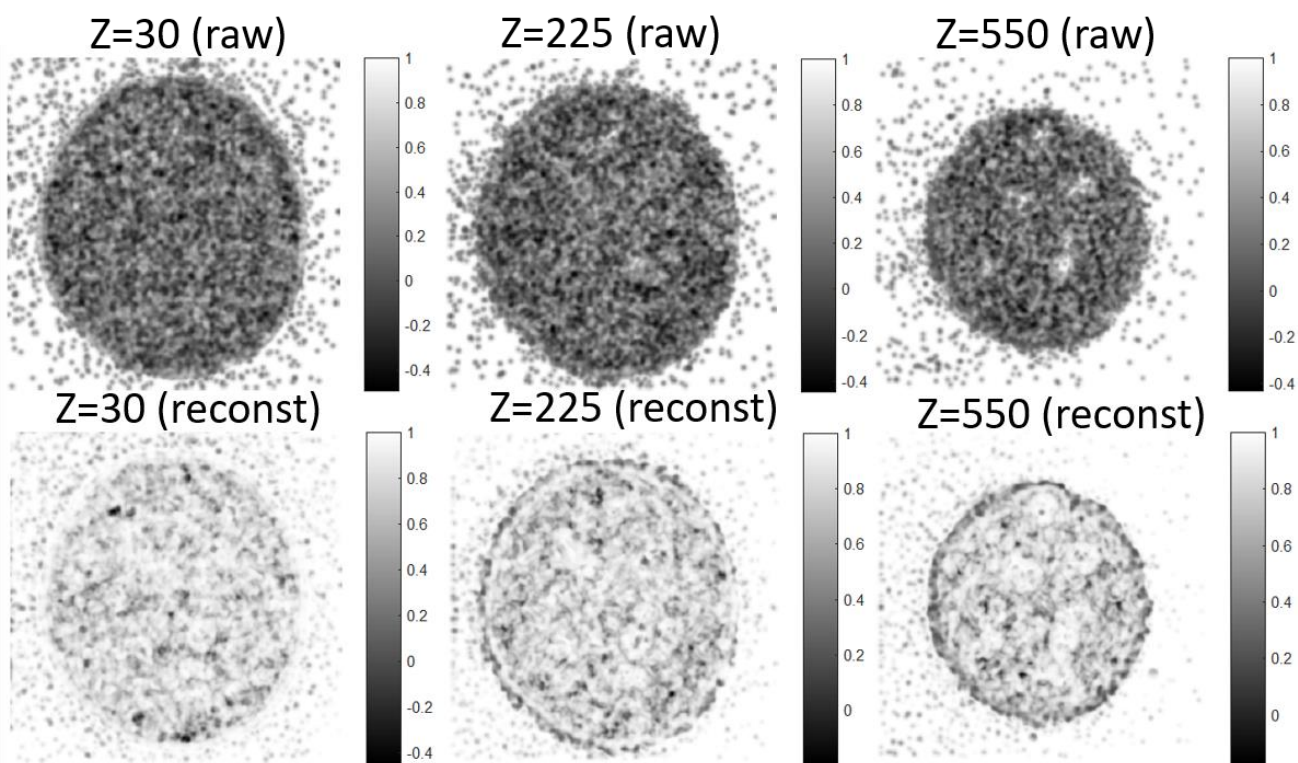
Confocal: Digitally deconvolved images on binned sections.

3D Renders from the reconstructed ion beam tomographic slices from two different viewing angles.

The high quality of final images compared to the initial ion images demonstrated the benefit of the presented mathematical analysis pipeline.

a**b**

Similarity index spatial maps



Supplementary Figure 18. Structural similarity index (SSIM) values were used to quantify the “similarity” measure of DNA images at the ^{127}I -dU and ^{81}Br -dU channels for the raw and reconstructed ion images that were presented in Fig. 3.

(a) Reconstructed DNA images exhibit significantly higher similarity (SSIM: $0.86 \pm \text{SE } 0.001$) compared to the raw DNA images ($0.54 \pm \text{SE } 0.0037$).

IBT-raw: SSIM values for measuring the similarity of the raw DNA images from ^{127}I -dU and ^{81}Br -dU.

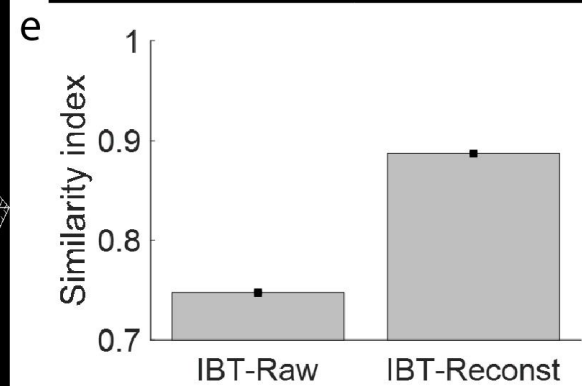
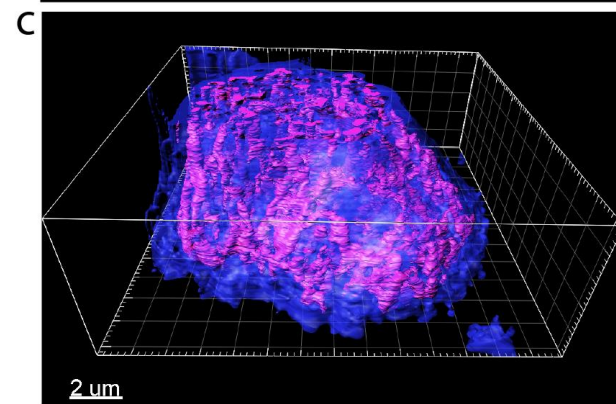
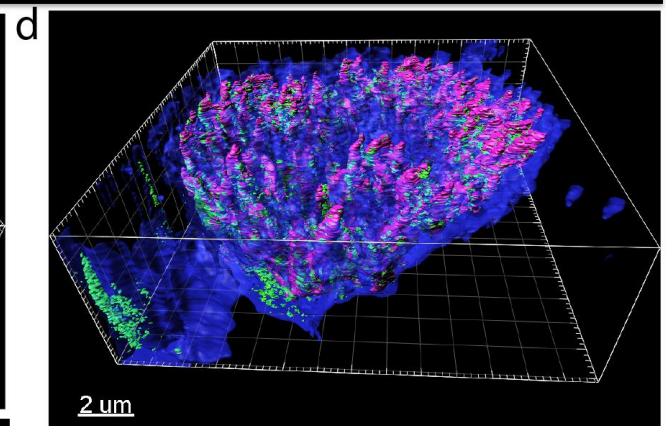
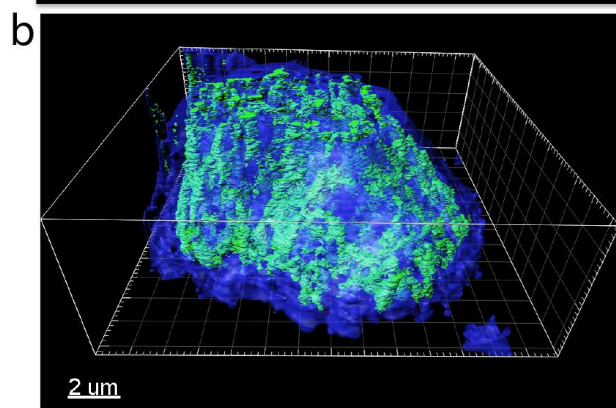
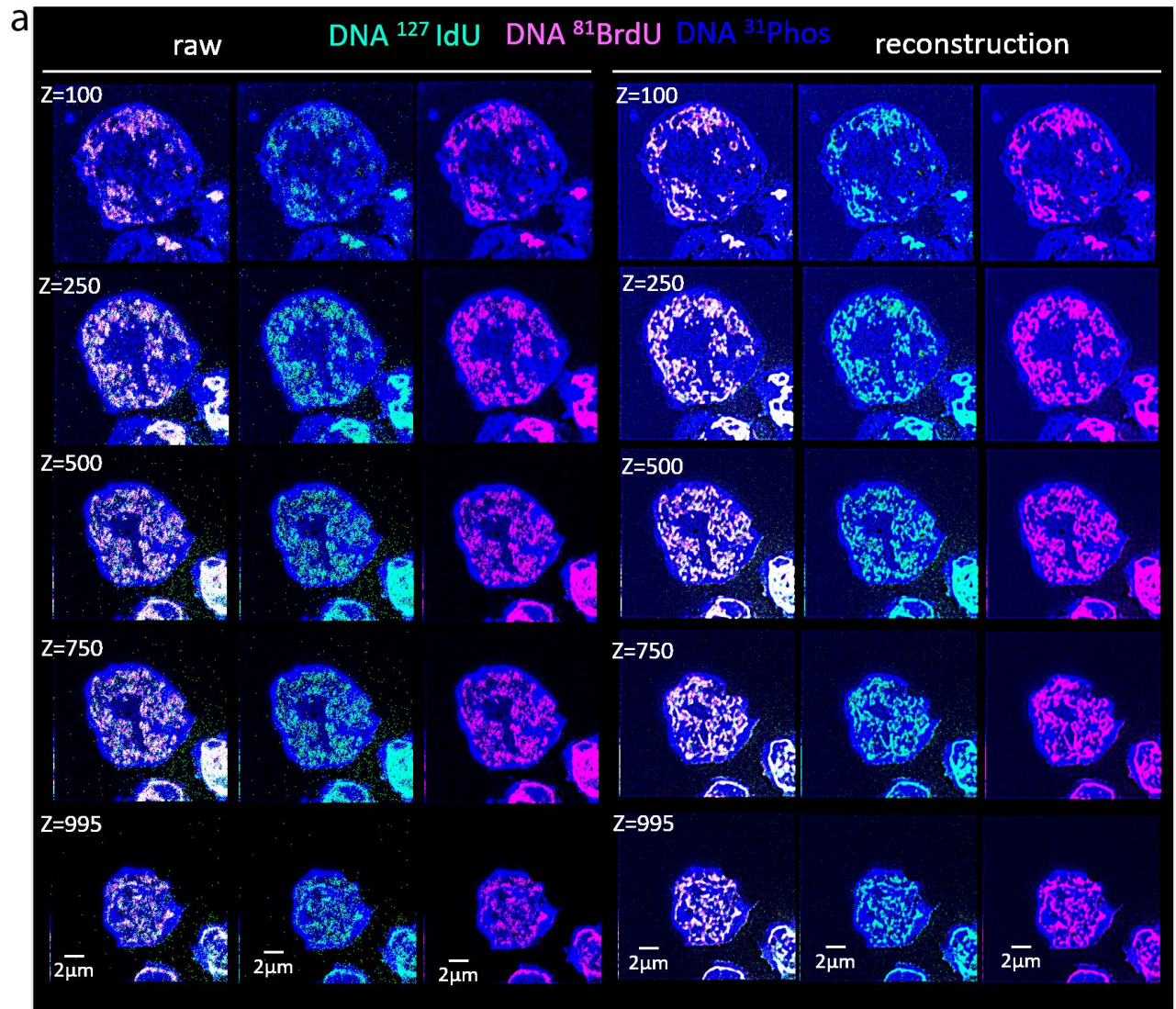
IBT-reconst: SSIM values for calculating the similarity of the reconstructed images from ^{127}I -dU and ^{81}Br -dU.

$n = 737$ sections were used in the bar graph with mean and standard error of SSIM values.

(b) Spatial map of SSIM quantification in DNA images for 30th, 225th, and 550th ion beam tomographic slices.

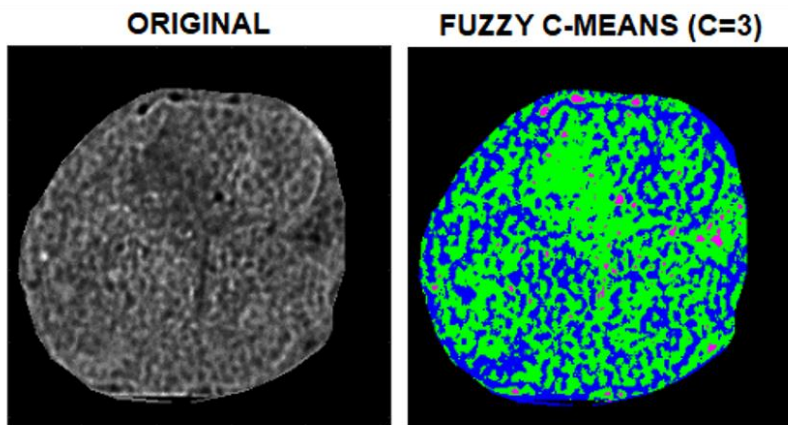
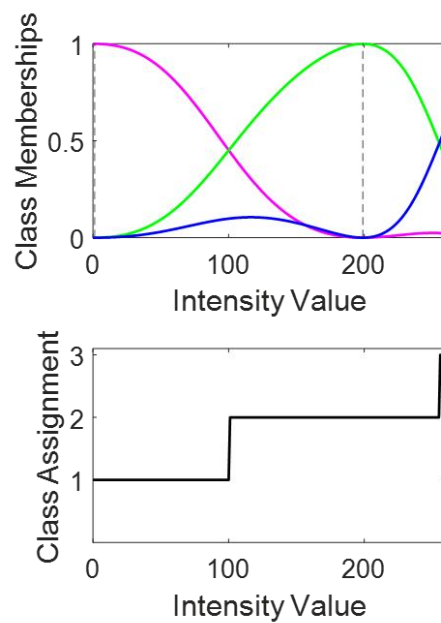
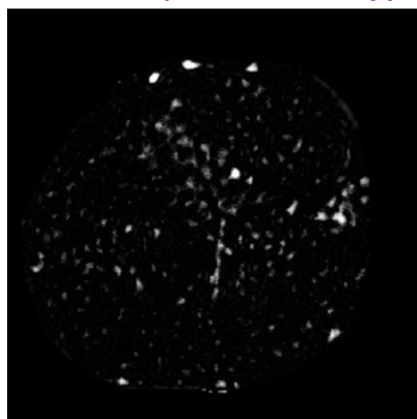
(Top row) SSIM index values per pixels were plotted as a spatial map for raw DNA images. Most pixels average around dark grey SSIM values, suggesting high dissimilarity.

(Bottom row) SSIM spatial values for reconstructed DNA images. Most pixels span around light grey SSIM values, providing high degree similarity between images.

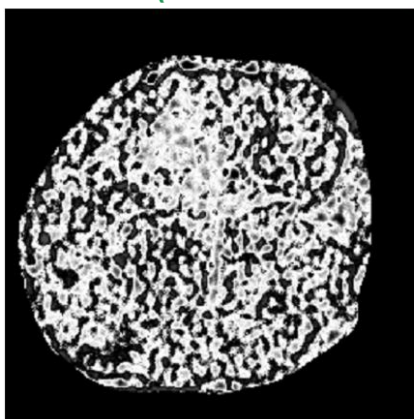


Supplementary Figure 19. SSIM values of DNA images at the ^{127}I -dU and ^{81}Br -dU channels for the raw and reconstructed ion images in a Nalm6 cell.

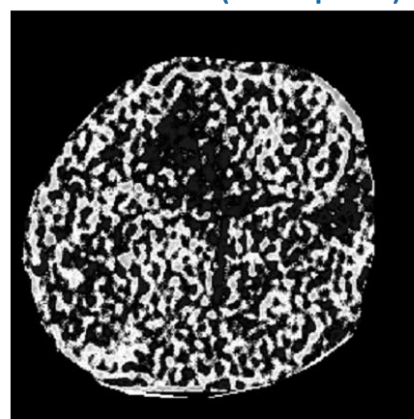
- (a) Similar to the Figure 3, but for Nalm6 cells. Raw images of replicated DNA (green and magenta) and largely chromatin (blue) are noisy and reconstructed images show spatially resolved patterns in the chromatin.
- (b) 3D renders of Nalm6 ion beam tomogram. Replicated DNA by ^{127}I -dU (green) and largely chromatin by ^{31}P (blue).
- (c) 3D visualization of Nalm6 with Replicated DNA by ^{81}Br -dU (magenta) and largely chromatin by ^{31}P (blue).
- (d) Inverted 3D position of the same Nalm6 cell with ^{127}I -dU (green), ^{81}Br -dU (magenta), and chromatin by ^{31}P (blue).
- (e) Reconstructed chromatin images exhibit higher similarity (SSIM: $0.88 \pm \text{SE } 0.001$) compared to the raw DNA images ($0.74 \pm \text{SE } 0.001$).

a**b****c** Class 1 (Low density)

Class 2 (Decondensed)



Class 3 (Compact)



Supplementary Figure 20. Fuzzy logic segmentation in a B cell lymphoblast for 50th slice.

(a) Original image (improved by mathematical pipeline) was used for segmentation process. A fuzzy C-means clustering (C=3) was calculated for the ³¹P image based on intensity values.

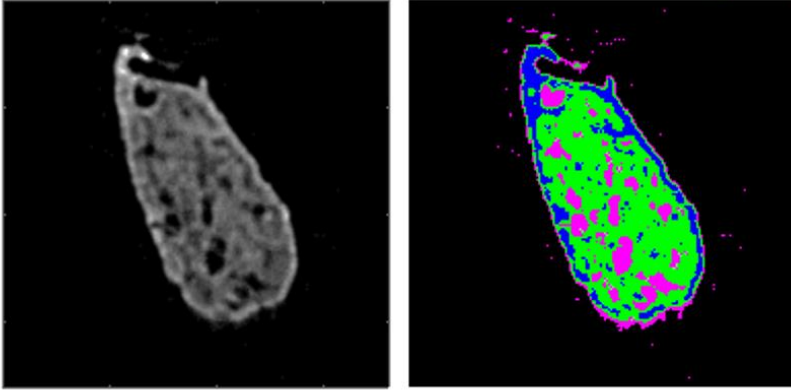
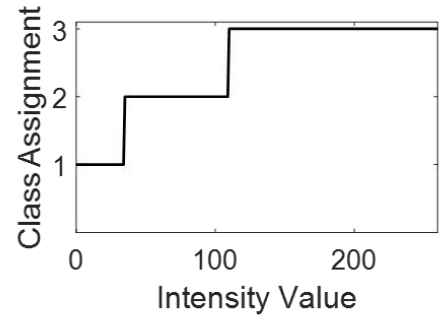
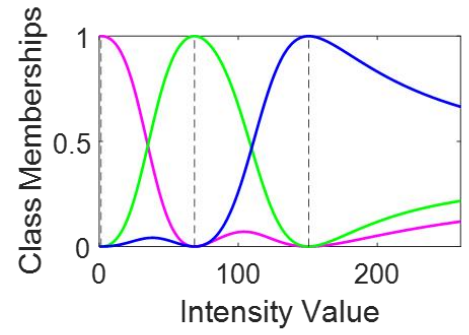
(b) Pixel values were sorted into class memberships based on density of chromatin distribution.

(c) Each ion image corresponding to the assignments of class 1 (low chromatin density), class 2 (decondensed chromatin), and class 3 (compact chromatin).

a

ORIGINAL

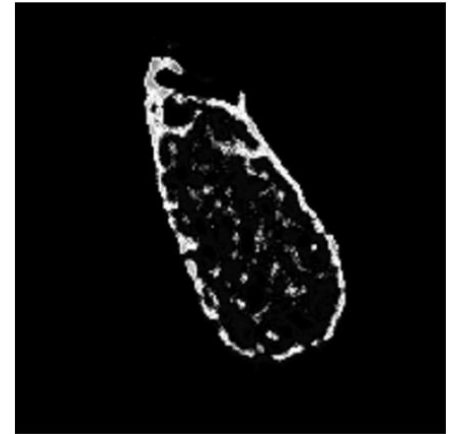
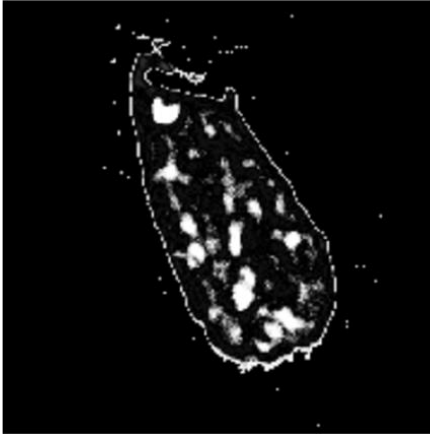
FUZZY C-MEANS (C=3)

**b****c**

Class 1 (Low density)

Class 2 (Decondensed)

Class 3 (Compact)



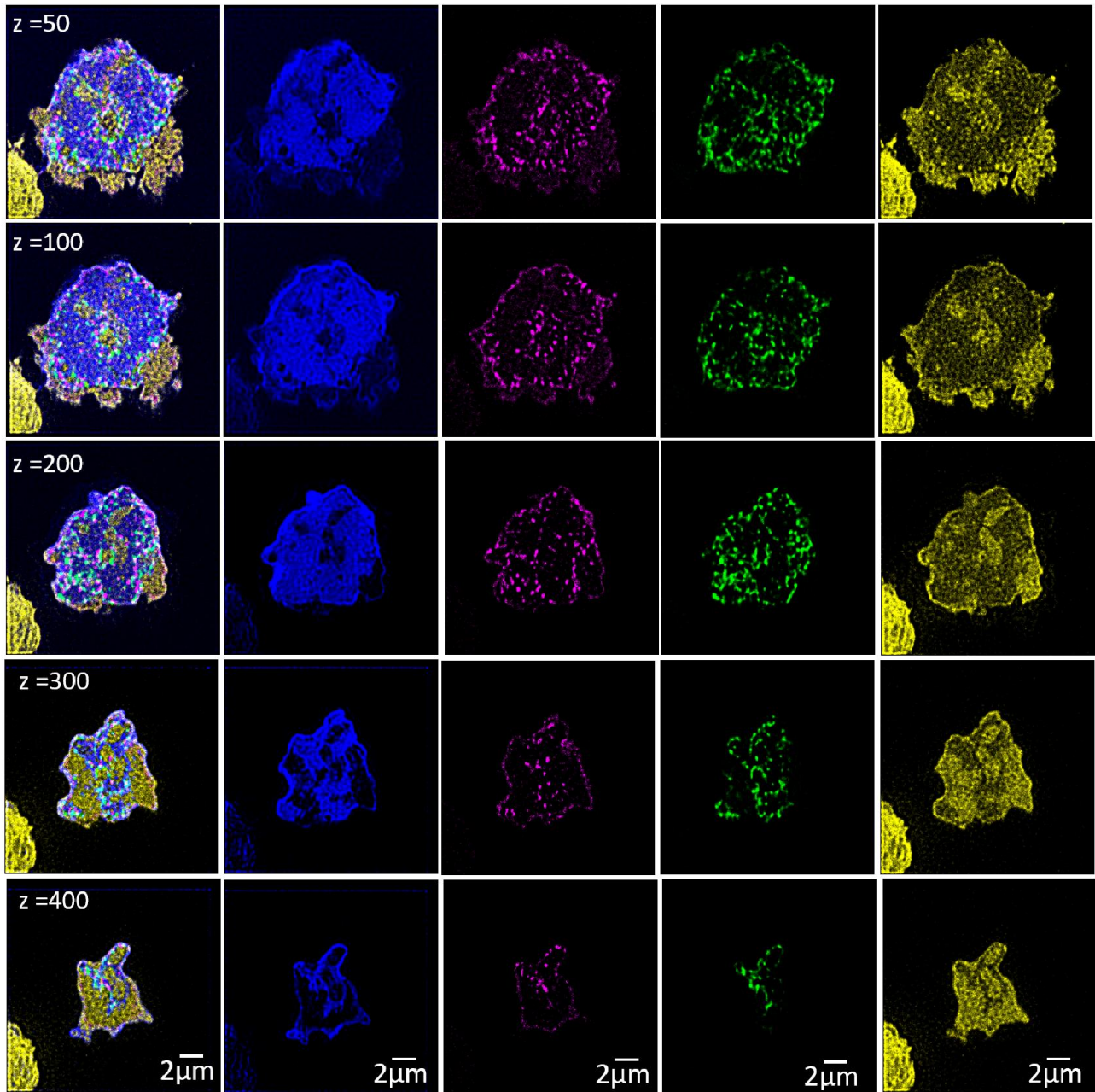
Supplementary Figure 21. Fuzzy logic segmentation in a HeLa cell for 500th slice.

Similar to the previous Supplementary Figure 15,

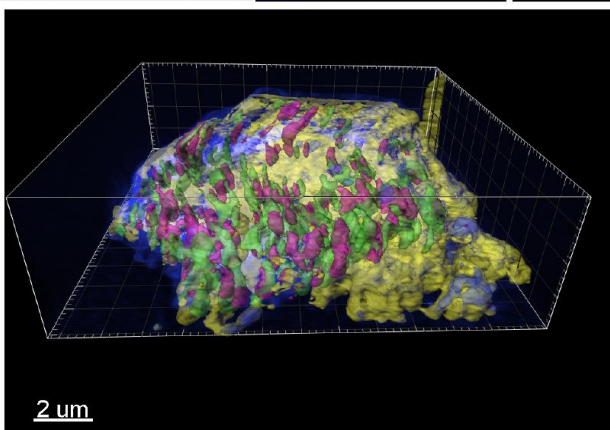
- (a) C-means clustering (C=3) was used to sort the pixel values,
- (b) class assignments for three density levels of chromatin, and
- (c) segmented images of chromatin for classes 1-3.

Instead of using direct calculation of intensity values, Fuzzy C-means based clustering of ion images provided determination of chromatin states without manually changing intensity threshold levels for segmentation.

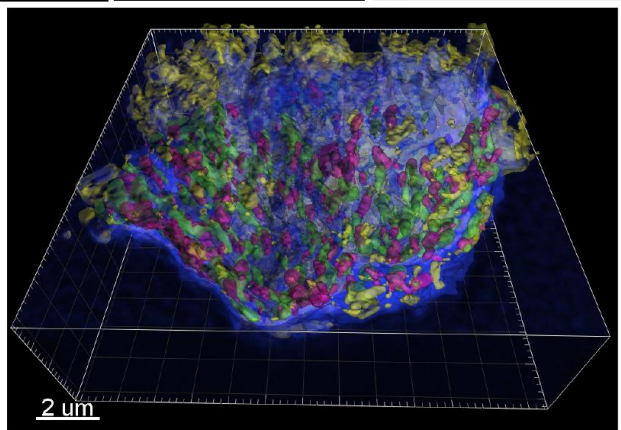
a ^{127}I -dU (1-h) 2-h chase ^{81}Br -dU(30-min) ^{31}P (DNA) ^{34}S (Protein)



b



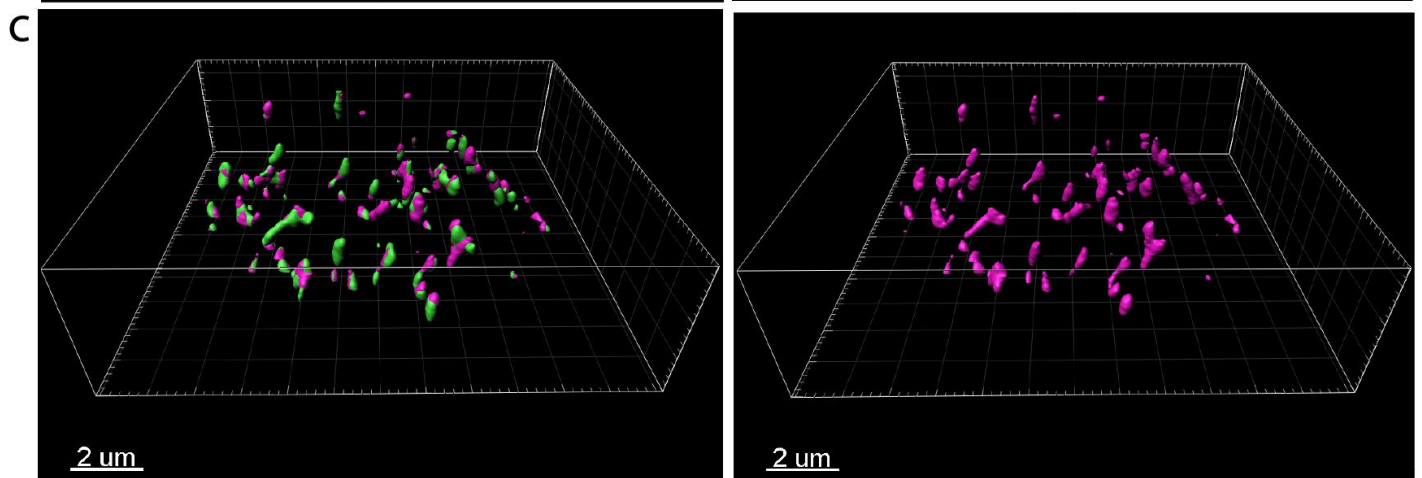
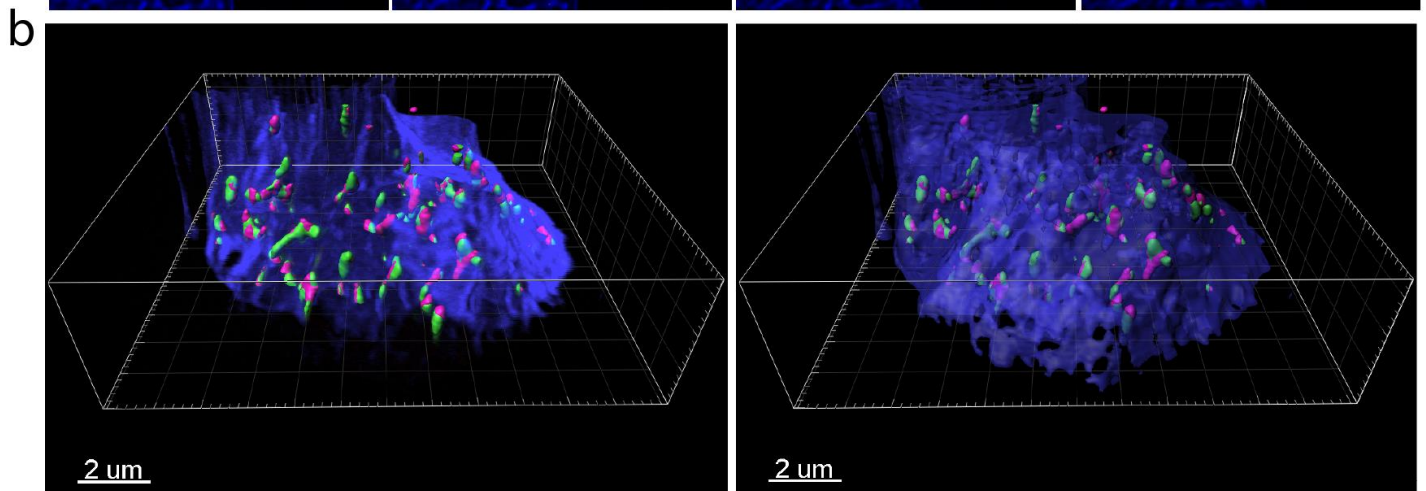
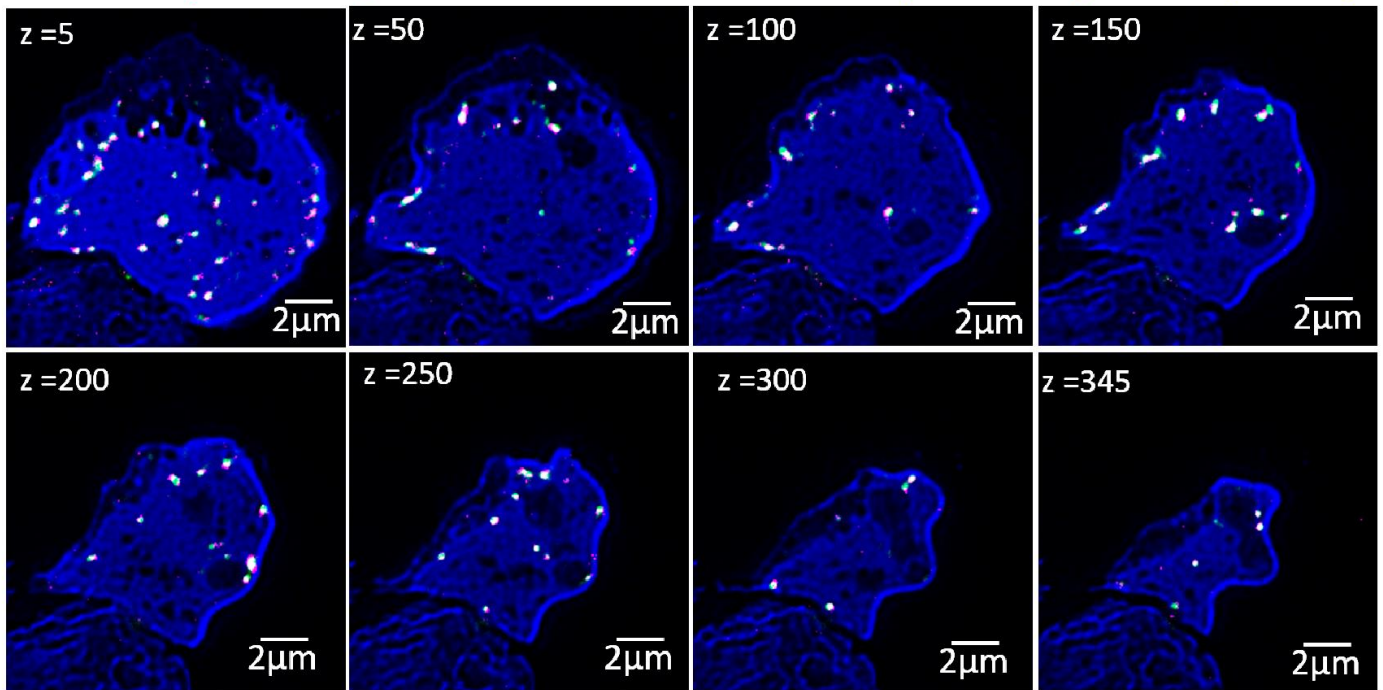
c



Supplementary Figure 22. Four channel representation of replication data in Figure 4 (2-h chase).

- (a) Nalm6 cell was pulsed with ^{127}I -dU (green) for 1 hour, and then chased in culture media for 2 hours, followed by a second pulse with ^{81}Br -dU (magenta) for 30 minutes. IBT image sections for 50th, 100th, 200th, 300th, and 400th slices were shown. ^{31}P (blue) was used for chromatin analysis. ^{34}S (yellow) was utilized as an indicator for protein concentration.
- (b) 3D visualization of 600 slices in a Nalm6 cell. Replication sites (green and magenta), chromatin (blue), and proteins (yellow). Higher concentration of replication forks was around the half bottom of the cell.
- (c) An inverted 3D renders of the same Nalm6 cell with four colors as denoted.

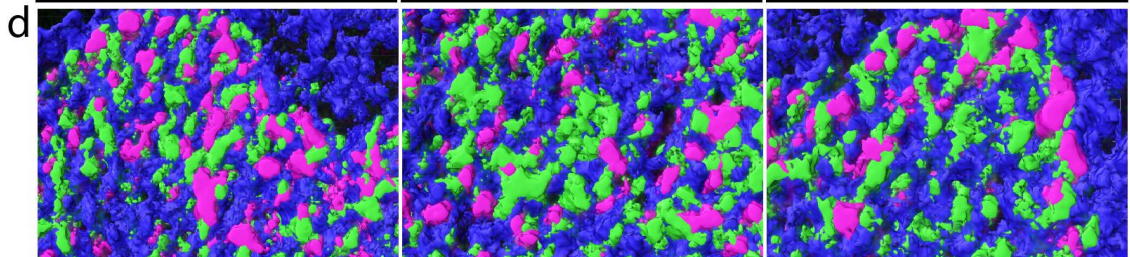
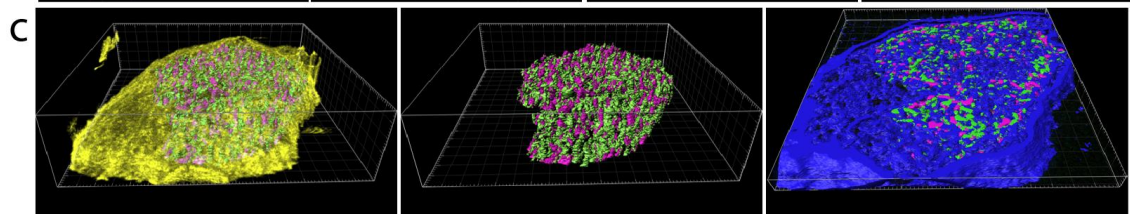
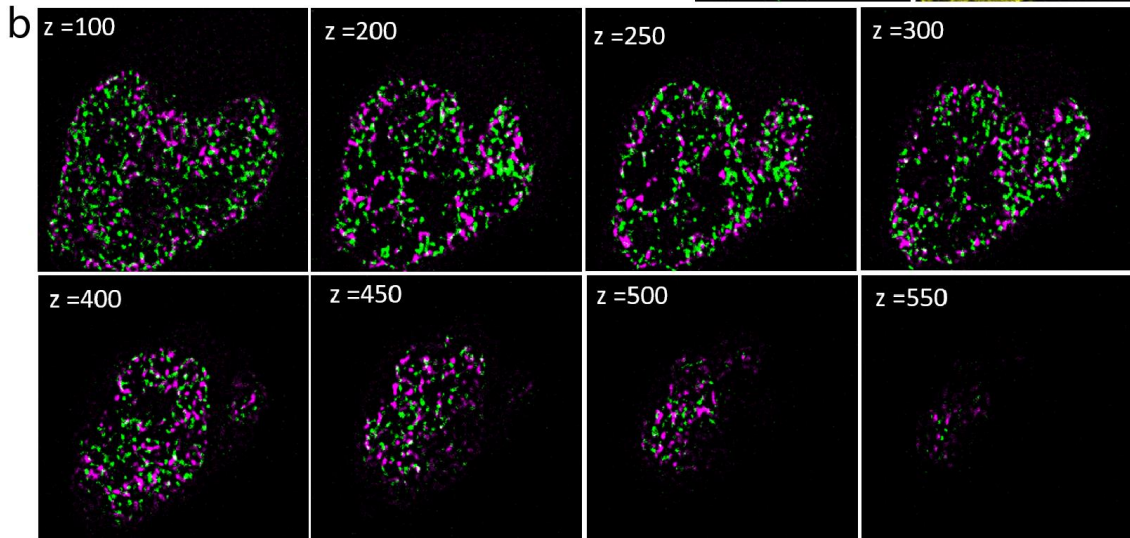
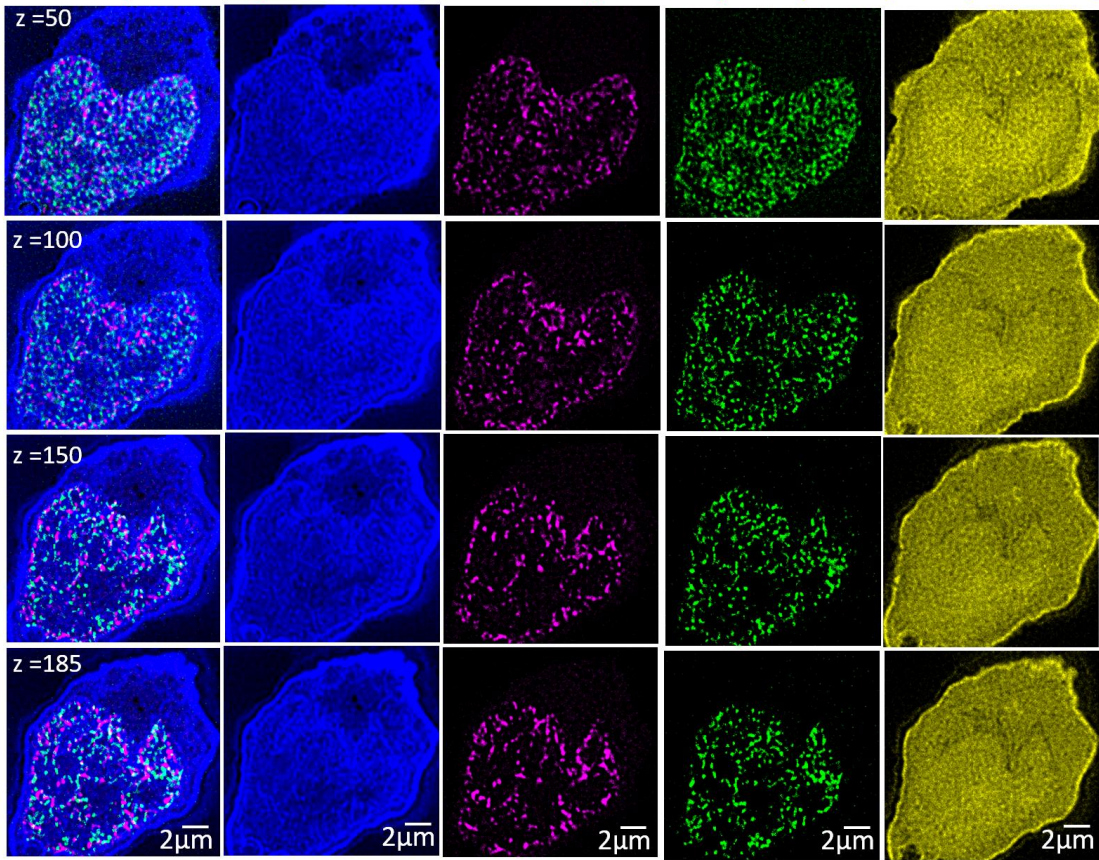
a ^{127}I -dU (30-min) 30-min chase ^{81}Br -dU(30-min) ^{31}P (DNA)



Supplementary Figure 23. Biological replicate experiment for replication dynamics in Figure 4 (30-min chase).

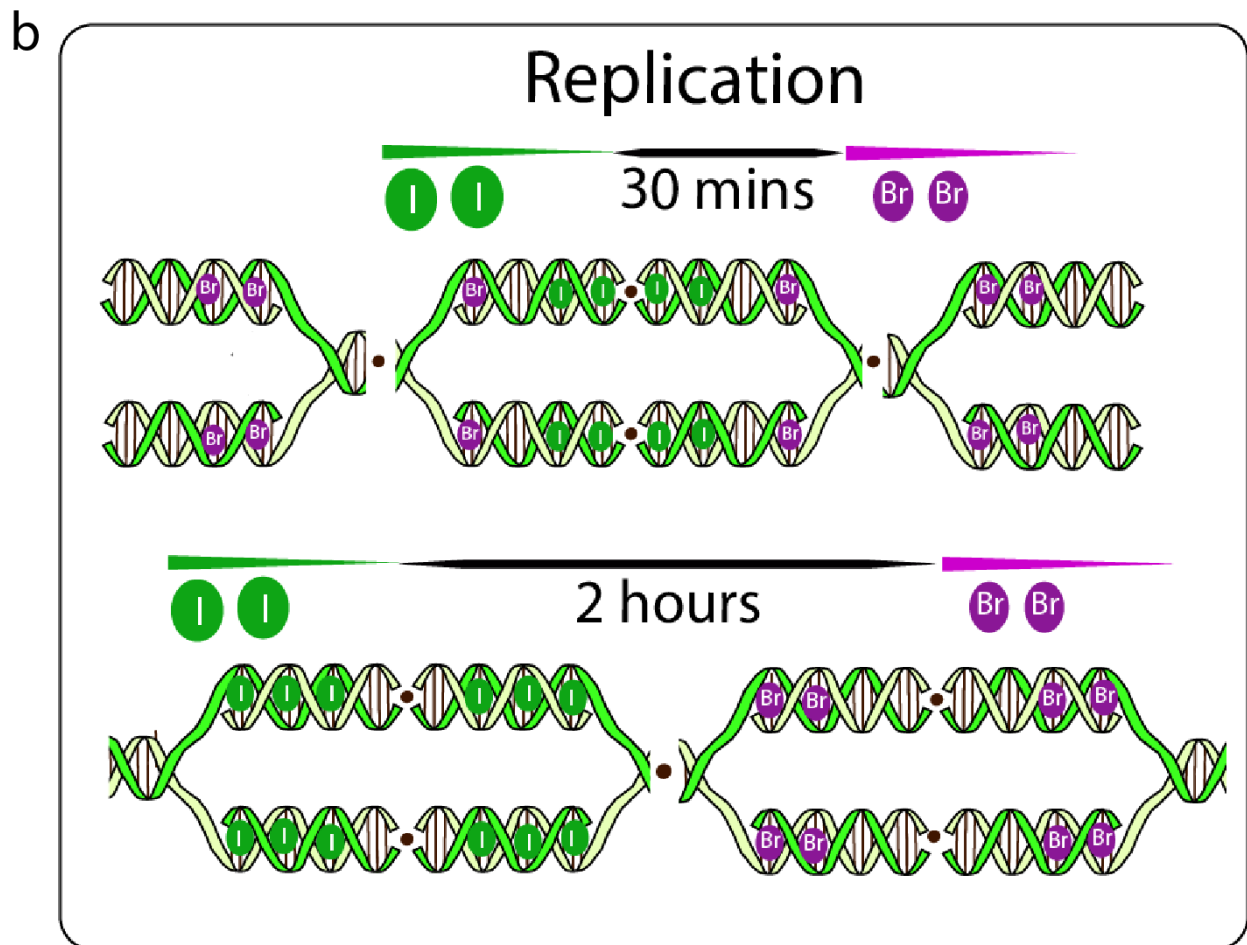
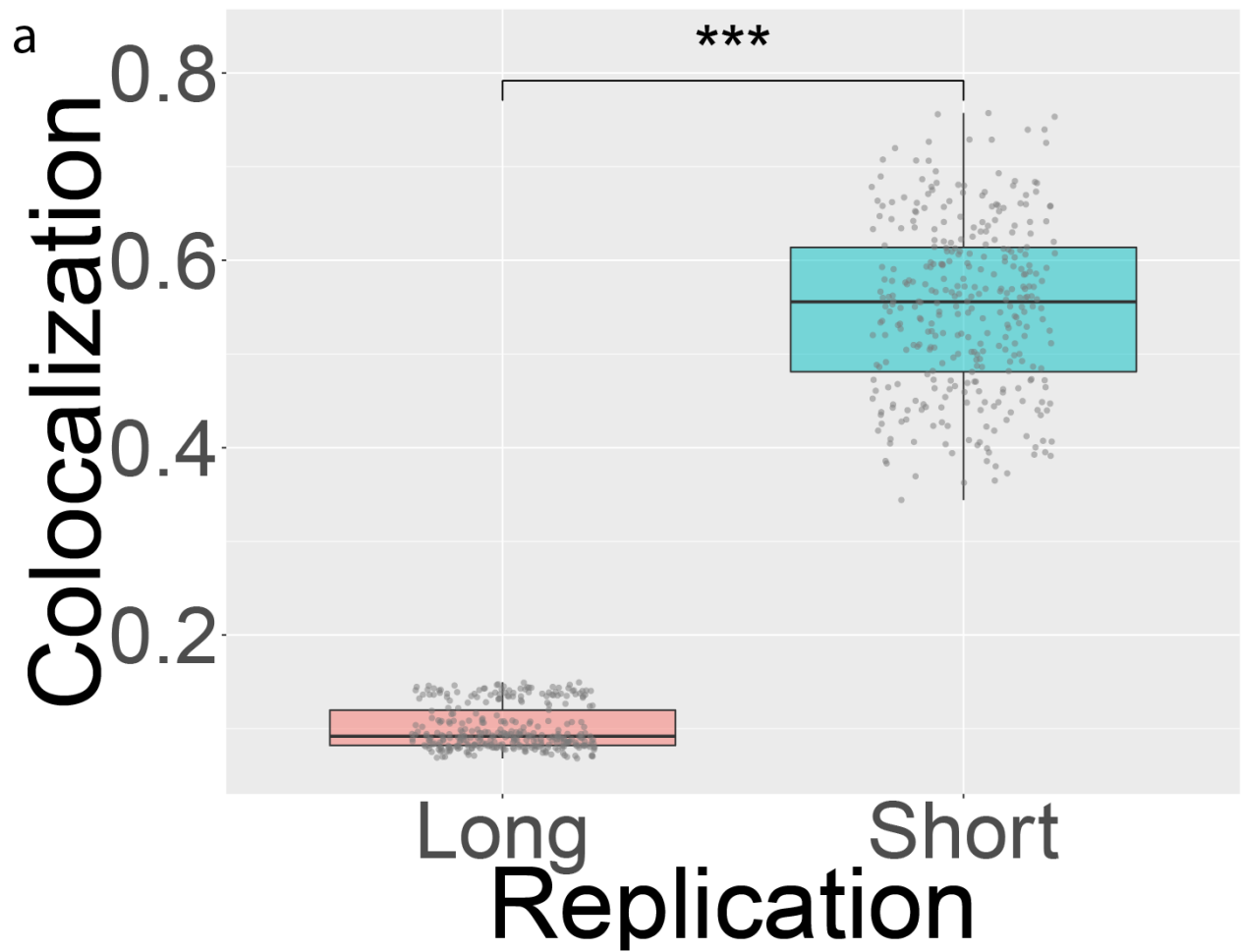
- (a) Nalm6 cell was pulsed with ^{127}I -dU (green) for 30 minutes, and then chased in culture media for 30 minutes, followed by a second pulse with ^{81}Br -dU (magenta) for 30 minutes. Digitally processed IBT image sections for 5th, 50th, 100th, 150th, 200th, 250th, 300th, and 345th slices were shown. ^{31}P (blue) was used to identify largely chromatin.
- (b) 3D renders of 350 sections in the Nalm6 cell. Surface function was used to colorize replication site images. The 31P channel was original data (left) and surface renders with 50%transperancy setting in the 3D render.
- (c) Only replication forks (green and red) were highlighted in 3D, showing significant overlaps and variability in spatial distribution in cellular volumes.

a ^{127}I -dU (30-min) 2-h chase ^{81}Br -dU(30-min) ^{31}P (DNA) ^{34}S (Protein)



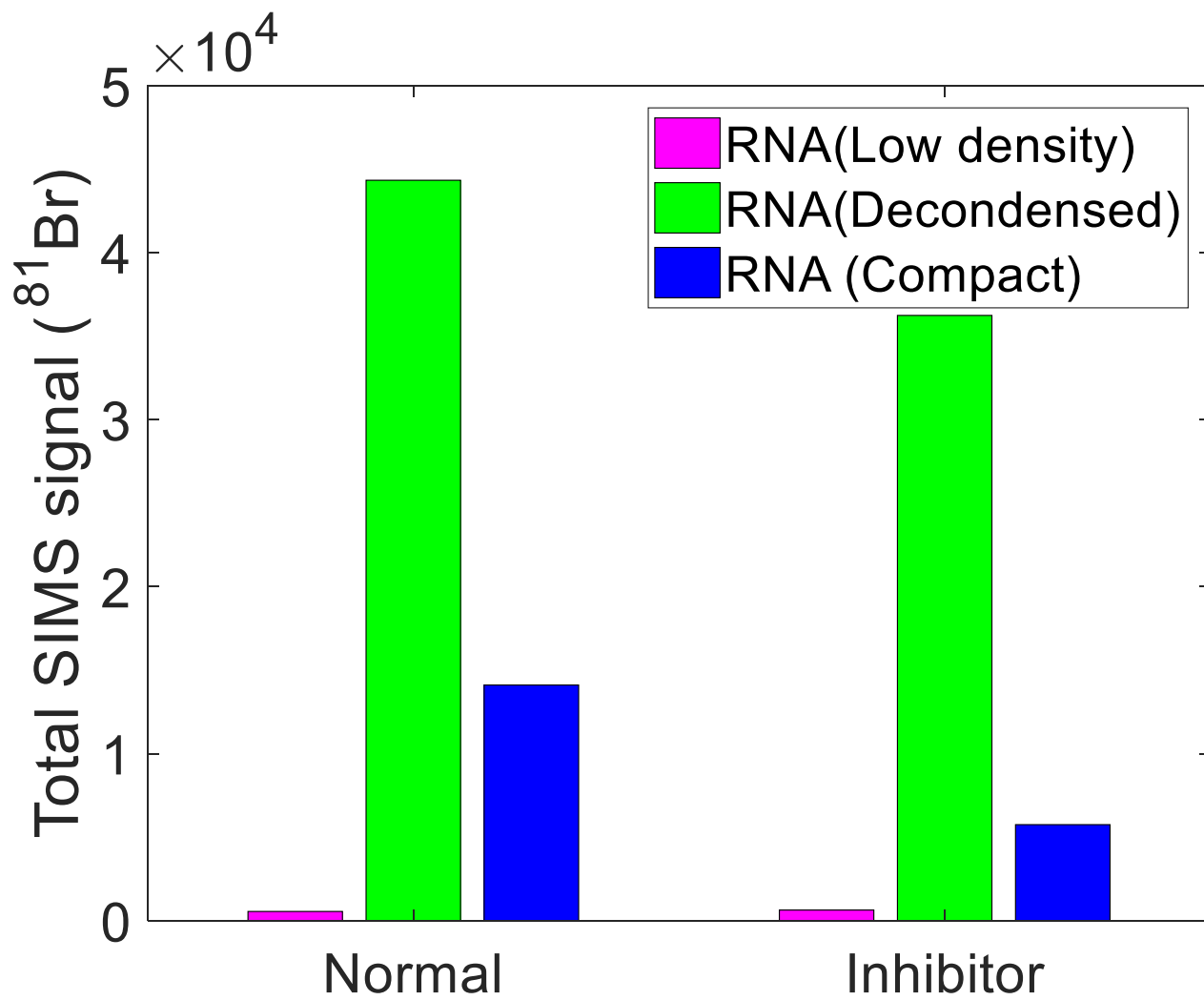
Supplementary Figure 24. Biological repeat for replication dynamics in Figure 4 (2-h chase).

- (a) Nalm6 cell was pulsed with ^{127}I -dU (green) for 30-min, and then chased in culture media for 2 hours, followed by a second pulse with ^{81}Br -dU (magenta) for 30 minutes. IBT image sections for 50th, 100th, 180th, and 185th slices were shown. ^{31}P (blue) was used for chromatin and ^{34}S (yellow) was imaged for proteins.
- (b) Overlaps of replication forks are minimal. 2D sections from 100th, 200th, 250th, 300th, 400th, 500th, and 550th ion images.
- (c) 3D renders of 600 slices in a Nalm6 cell. Replication sites (green and magenta), proteins (yellow), and chromatin (blue).
- (d) Zoomed images from chromatin and replication forks, extracted from a 3D renders with 185 slices.



Supplementary Figure 25. Spatial overlaps of replication forks were higher in short chase experiments.

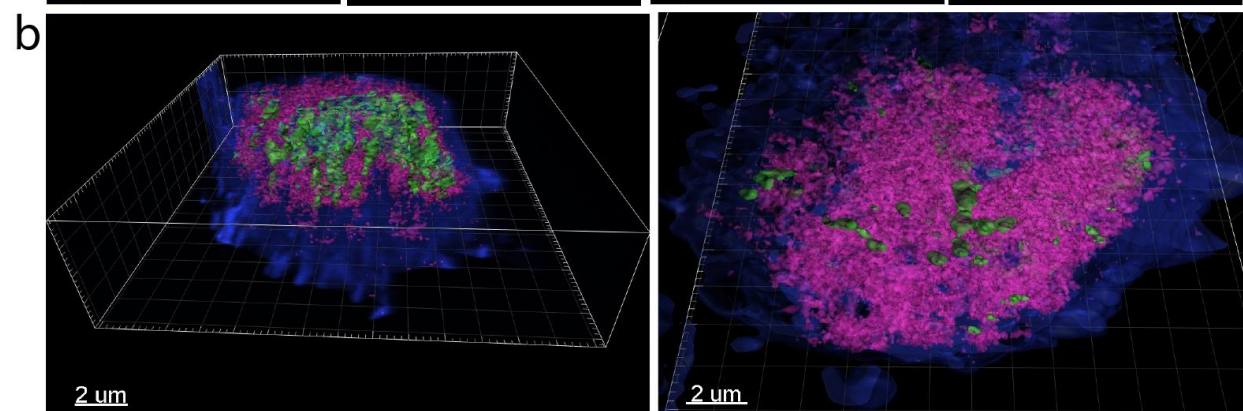
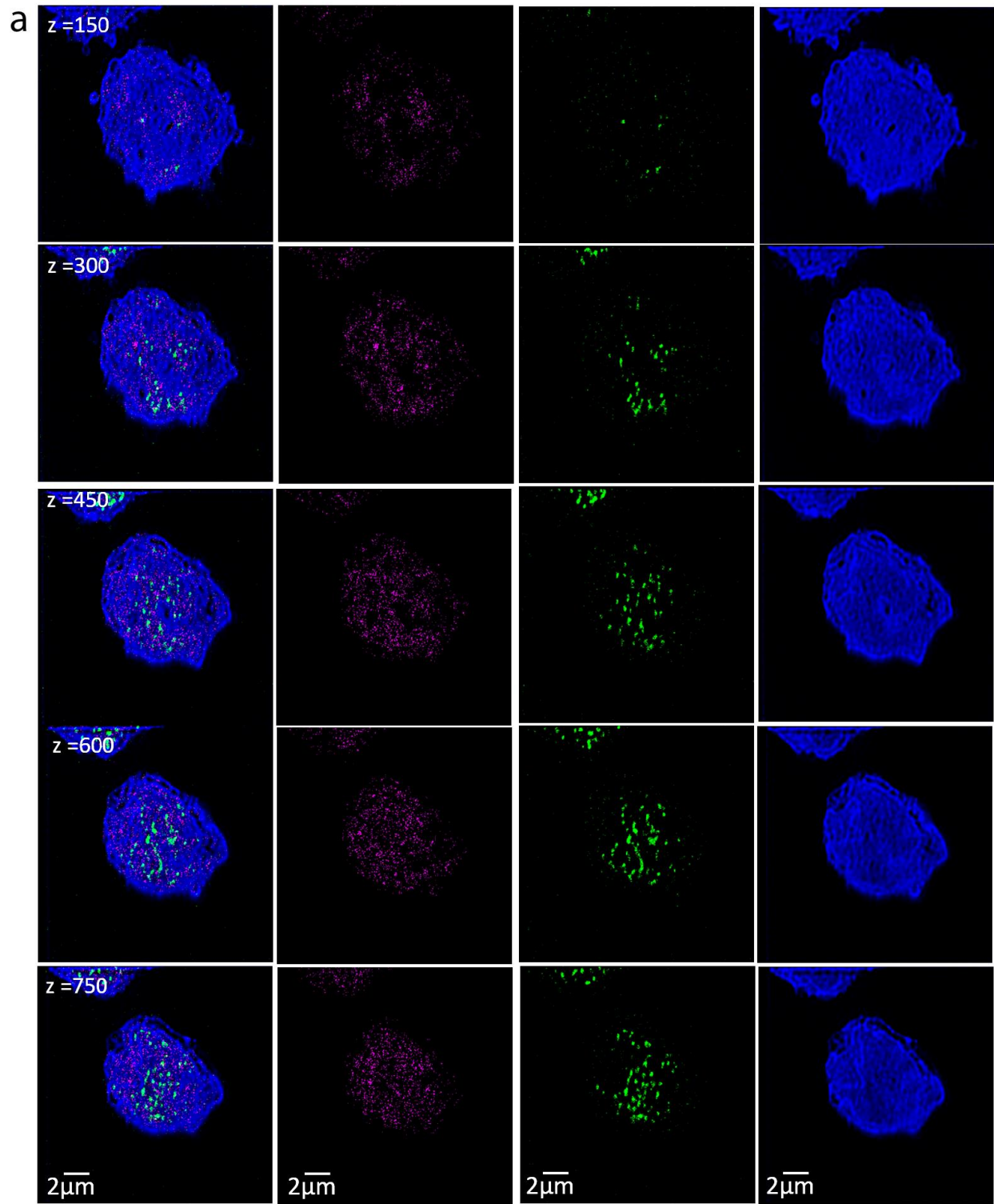
- (a) Correlation coefficient (CC) of 30-min chase experiments (from Supplementary Fig. 23) and 2-h chase experiment (from Supplementary Fig. 24) was computed. Long chase provided 0.55 CC and short chase exhibited 0.09 CC values, demonstrating the significantly more overlaps in 30-min compared to 2-h chase. Each dot corresponds to a single depth slice from the ion beam tomographic data.
- (b) Schematic model of spatial overlaps in replication dynamics. The first pulse (Green, ^{127}I -dU) and second pulse (^{81}Br -dU) occurs in similar replication loci when the time difference between the two is shorter.



Supplementary Figure 26. Newly synthesized RNAs are enriched in the decondensed region of the chromatin. 30 minutes of 81 Br-rU incorporation into Nalm6 cells.

Nascent RNA distribution at the 15th section of the first Nalm6 cell (Normal) showed high concentration in the decondensed region. Lower RNA concentration was in the compact and low-density chromatin regions.

In the existence of α -amanitin drug for 30 minutes after the RNA labeling in the second Nalm6 cell (inhibitor), newly synthesized RNA distribution was reduced in the decondensed as well as low density chromatin regions. Nascent RNA transcripts were partially repressed due to the degradation.

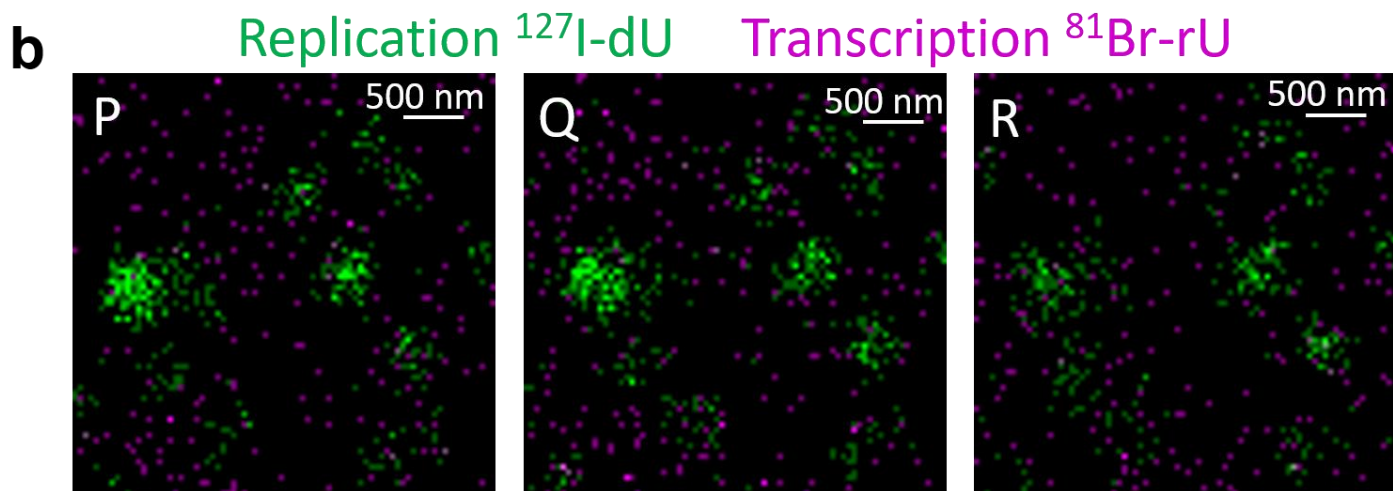
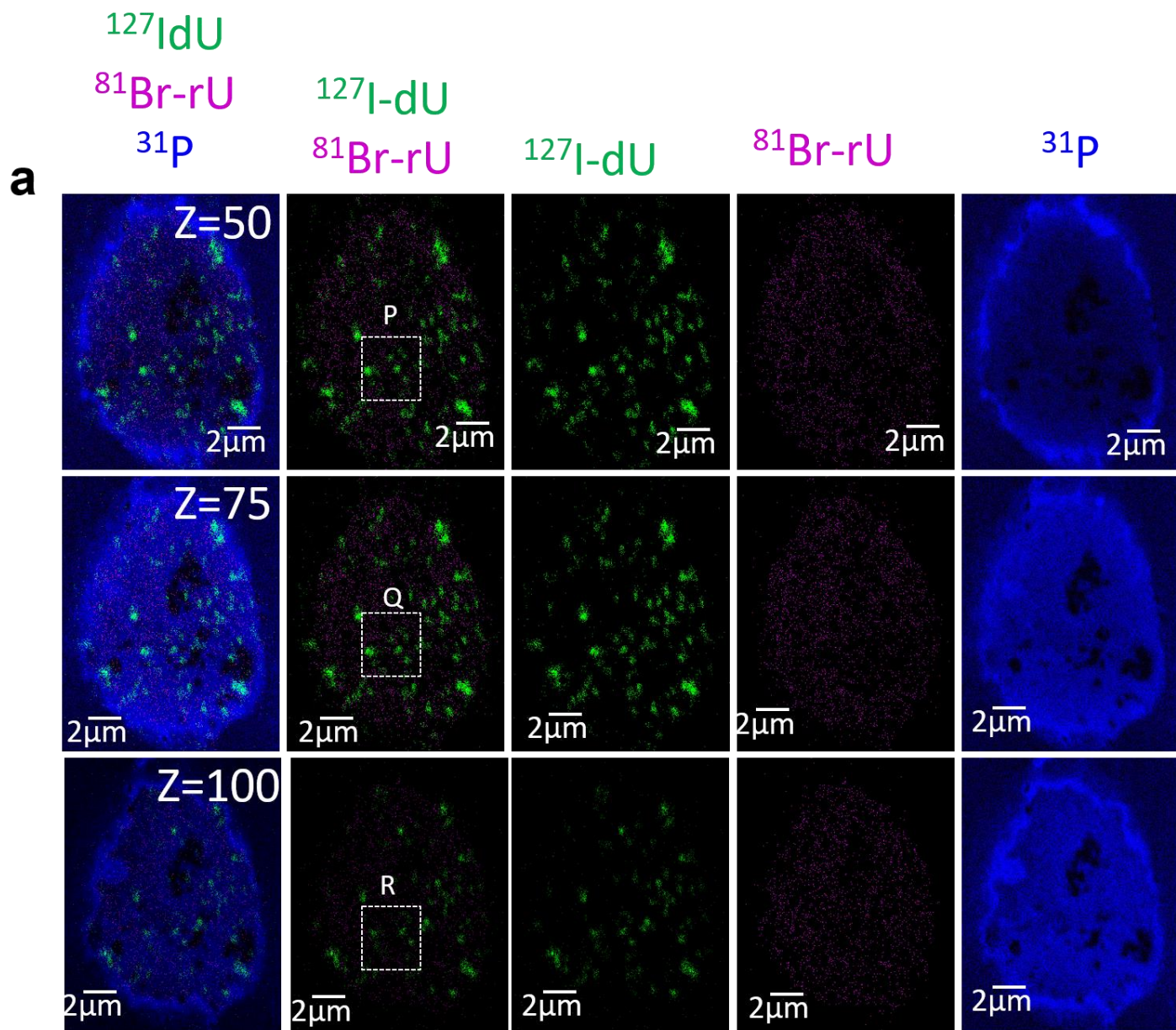


Supplementary Figure 27. Biological replicate data for nascent transcripts and replication (30-min pulse).

(a) Nalm6 cell was simultaneously incubated with ^{127}I -dU (green) to visualize replication and ^{81}Br -rU (magenta) to monitor transcription for 30 minutes. Tomographic ion slices for 150th, 300th, 450th, 600th, and 750th depths were presented. ^{31}P (blue) showed folding chromatin patterns.

(b) 3D renders of 750 slices for the Nalm6 cell. Replication sites (green), nascent transcripts (magenta), and chromatin (blue). Spatial isolation of RNA transcripts and replication forks was detected.

Note that spatial regions that look slightly darker in the rightmost column (chromatin) exhibited higher transcription, yielding a direct visualization of globally decondensed chromatin landscape.



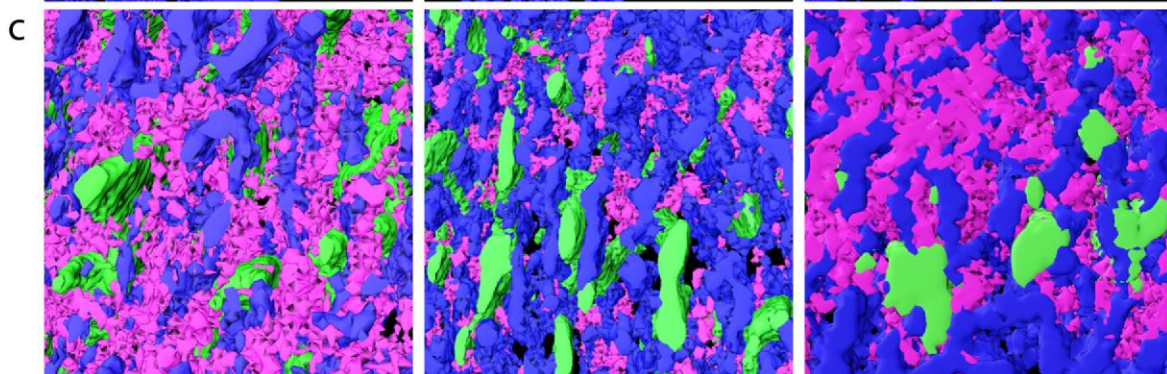
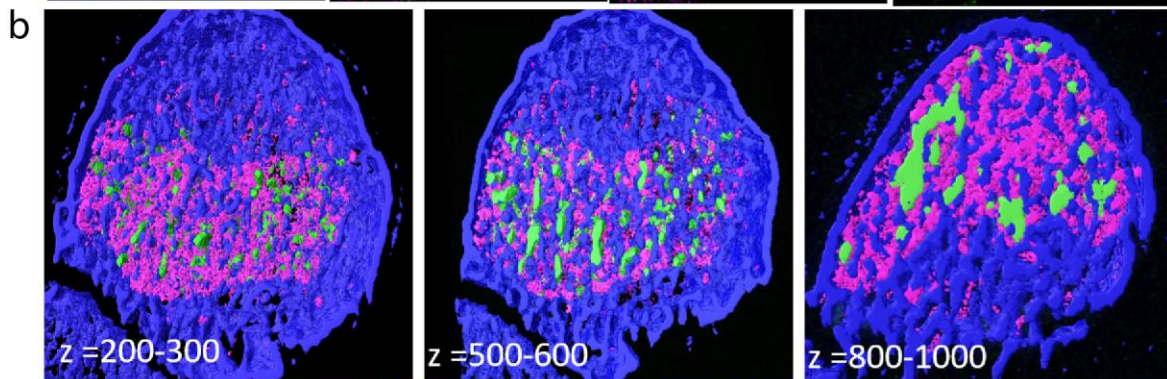
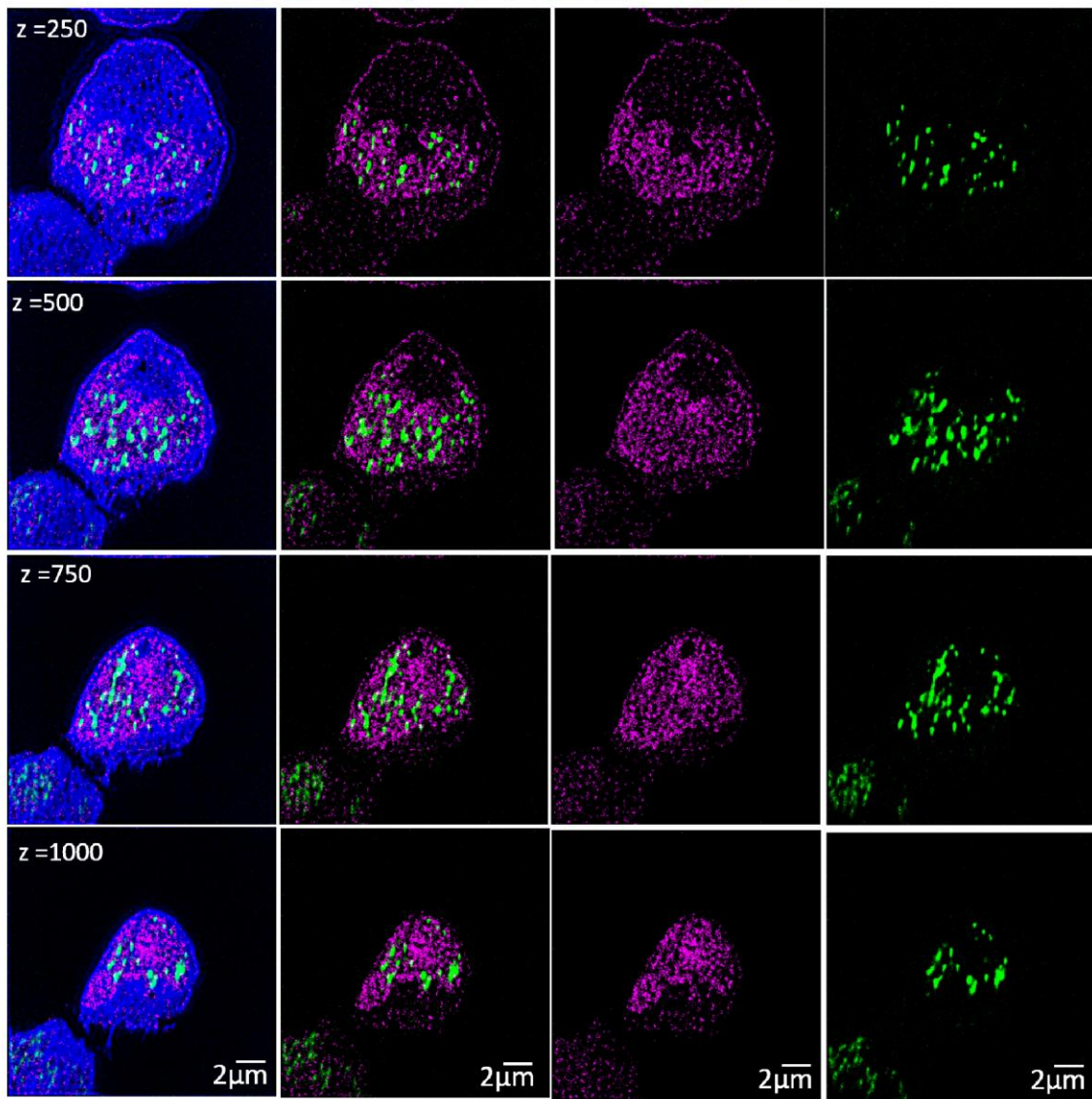
Supplementary Figure 28. Another replicate for simultaneous analysis of transcription and replication by IBT.

(a) Nalm6 cells were incubated with ^{127}I -dU and ^{81}Br -rU for 30 minutes in culture. Ion images for each channel was presented in each row for 50th, 75th, and 100th slices.

(b) Pixels from two distinct images for newly synthesized RNAs (magenta) and DNAs (green) do not overlap in the zoomed regions (P, Q, and R), demonstrating a spatial segregation of transcription and replication.

Note that these images were not processed by the mathematical pipeline, rather raw images are presented. 512x512 scans were used at 2 pA imaging current.

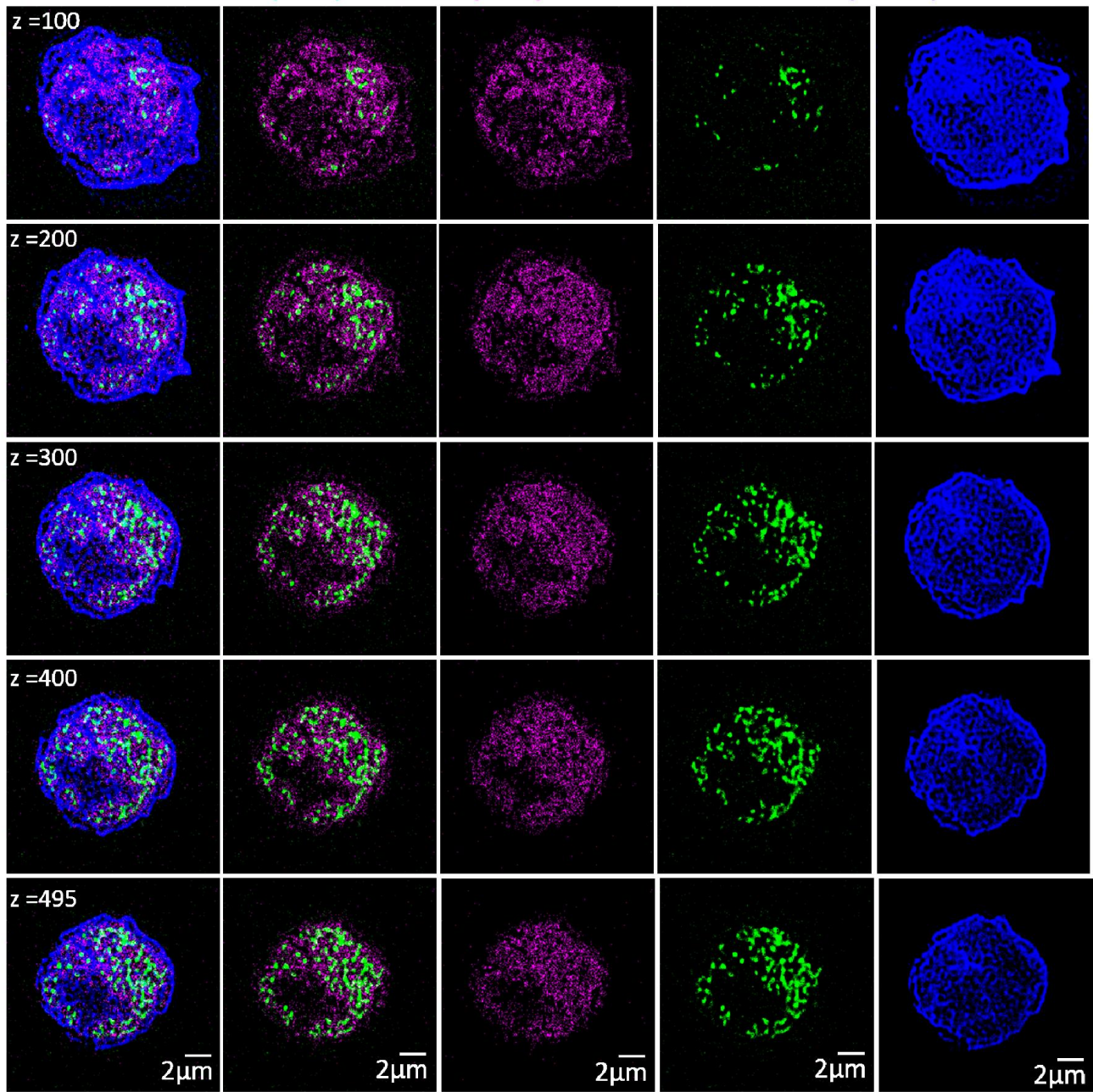
a ^{127}I -dU (2-h) ^{81}Br -rU(2-h) ^{31}P (DNA)



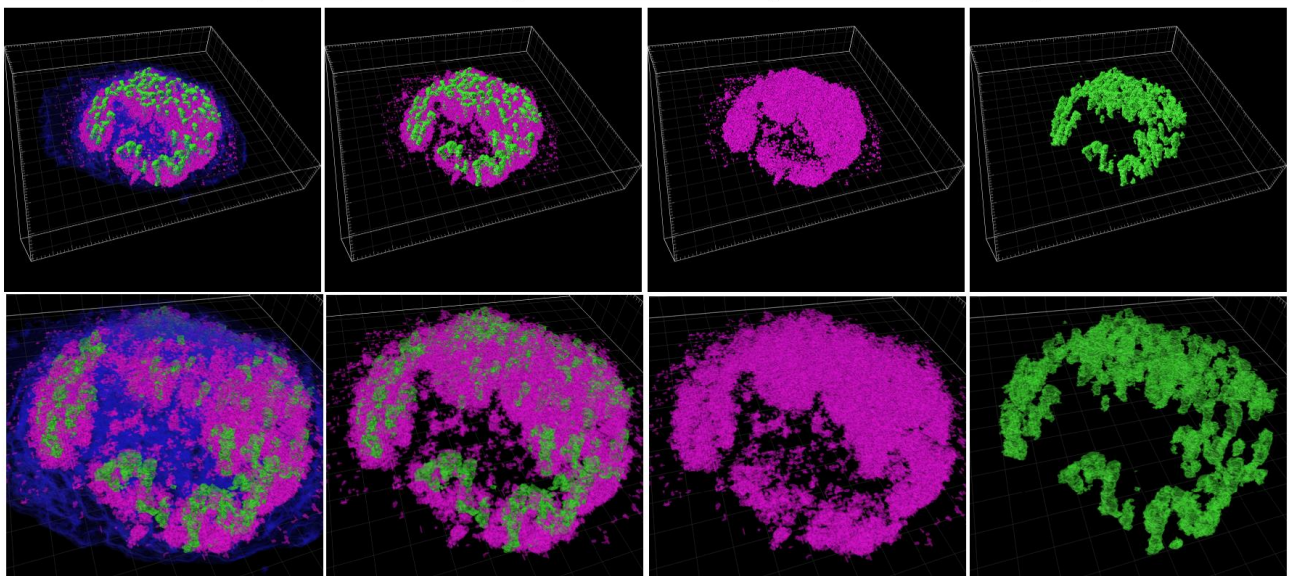
Supplementary Figure 29. Visualization of transcription and replication after 2-h pulse with ^{127}I -dU and ^{81}Br -rU.

- (a) Digitally processed images for IBT at 250th, 500th, 750th, and 1000th slices. Chromatin was detected at ^{31}P (blue), replication forks by ^{127}I -dU (green) and nascent transcripts by ^{81}Br -rU channel (magenta). Long incubation time led to longer replication sites and higher transcription signal. Spatial isolation of replication and transcription was preserved even at this long pulse experiment.
- (b) Partial 3D renders from more than 100 slices: 200-300, 500-600, and 800-1000 depths. Chromatin patterns and the spatial distribution of newly synthesized RNA and DNA around original chromatin were visualized.
- (c) Zoomed images from previous 3D renders. Fine features of replication and transcription were detected. Spatial segregation model is further validated in these images from 2-h incorporation of metabolic labeling.

a ^{127}I -dU (2-h) ^{81}Br -rU(2-h) w/ α -amanitin ^{31}P (DNA)



b



Supplementary Figure 30. Transcription inhibition during the labeling by α -amanitin for 2 hours at 10 μ M.

- (a) Visualization of transcription (magenta) by $^{81}\text{Br-rU}$, replication (green) by $^{127}\text{I-dU}$, and chromatin (blue) by ^{31}P signal. Processed ion images from 100th, 200th, 300th, 400th, and 495th slices were presented.
- (b) 3D Renders of transcription and replication around chromatin at a viewing angle. Top row corresponds to solid surfaces and bottom row shows partially transparent surfaces in the IBT images.

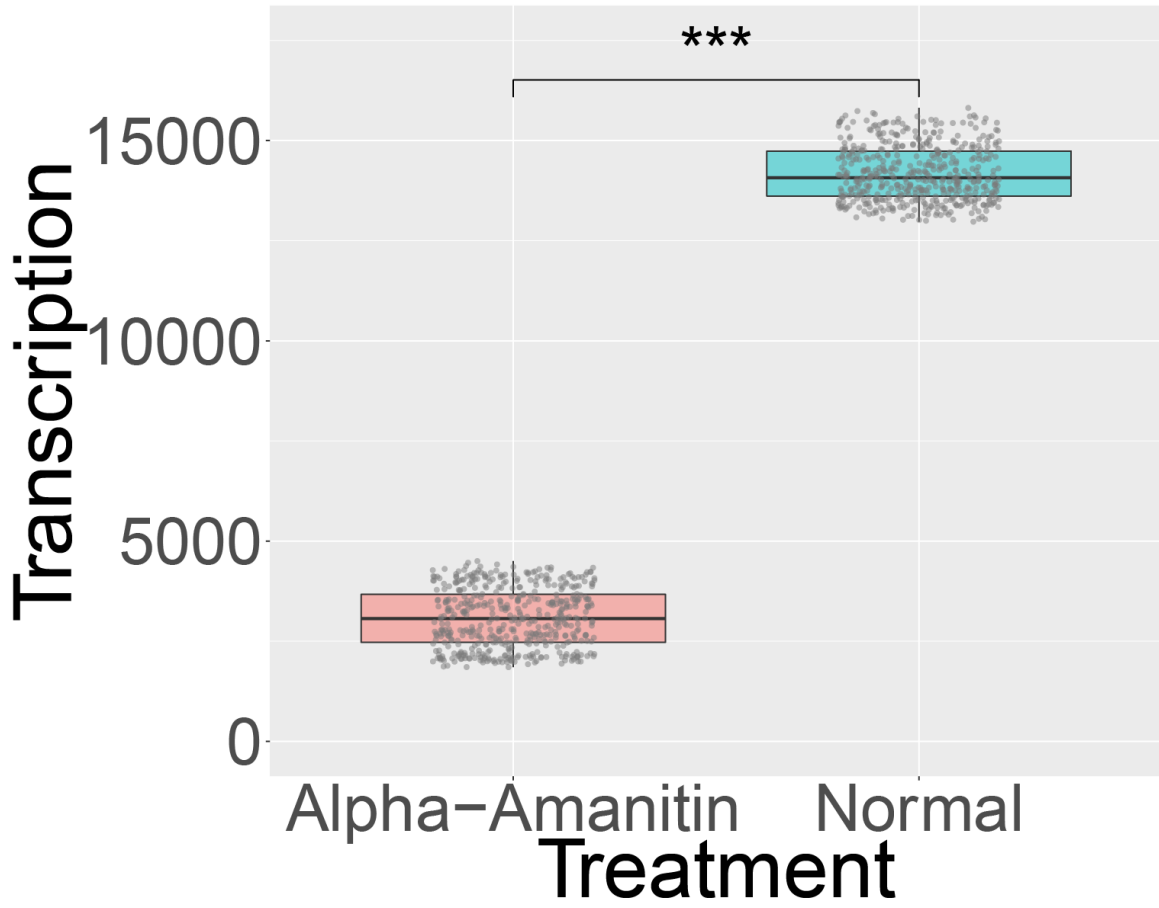
Spatial distribution of replication and distribution was consistent with previous results:

- Isolation of transcribing DNA and replicating DNA in 3D.
- Enrichment of transcription in decondensed chromatin regions.

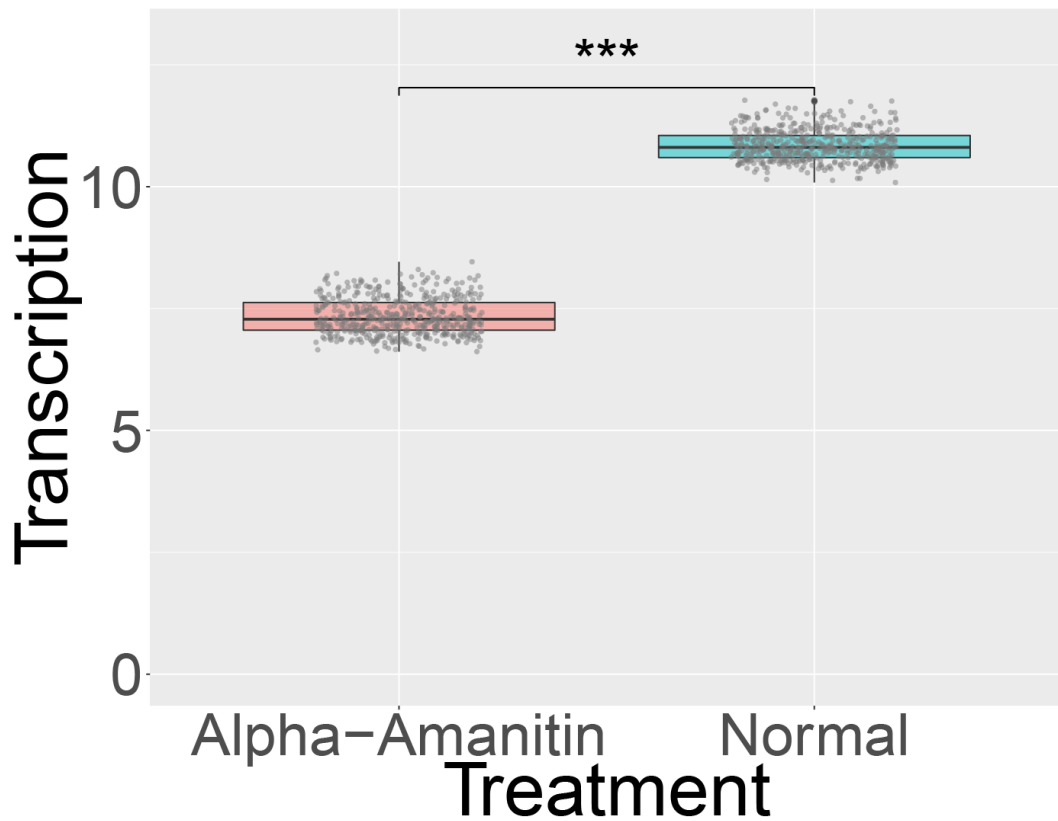
The effect of α -amanitin in active transcription:

- Total transcription signal reduced compared to the Supplementary Fig. 29 (same conditions, 2-h).
- Partial repression but not total transcription block.
- Replication did not get affected from transcription inhibitors.

a Unnormalized transcription signal after inhibition

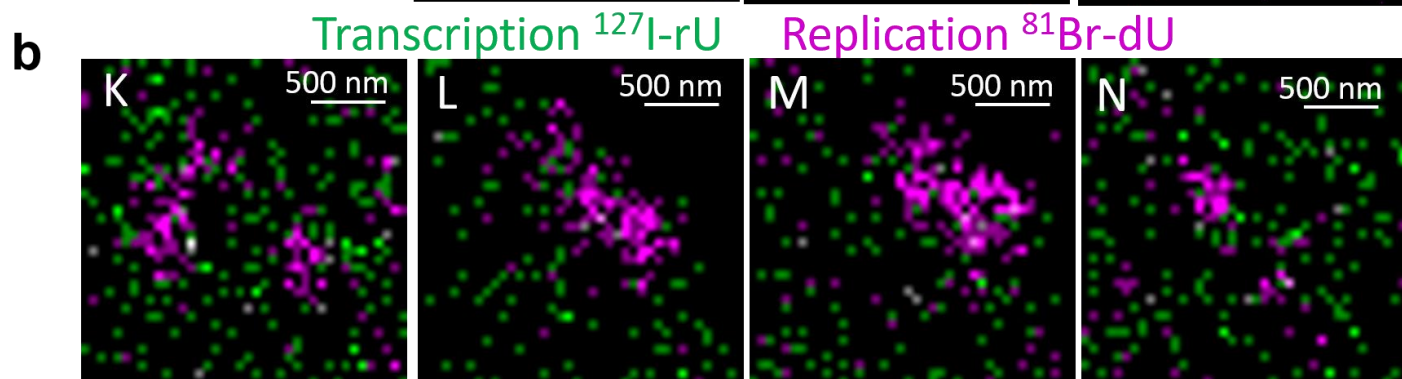
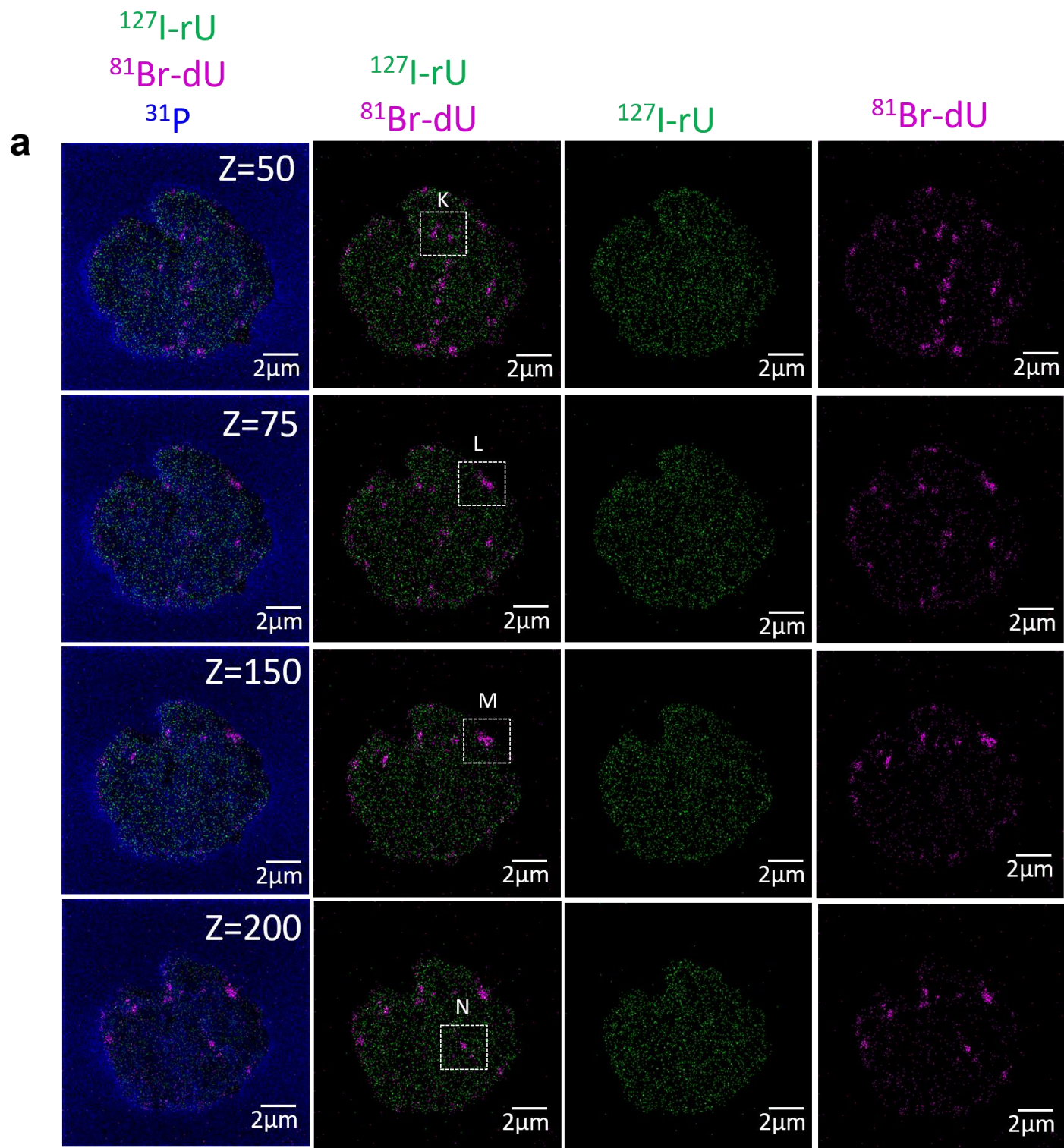


b Normalized transcription signal after inhibition



Supplementary Figure 31. Transcription inhibition reduced the nascent transcriptome signal.

- (a) Statistics of total transcription signal at the ^{81}Br -rU channel. Each data point corresponds to single depth from ion beam tomograms. It exhibited reduced signal down to the 0.21-fold of the transcription without inhibition. Each scatter point corresponds to single depth slice from ion beam tomographic dataset.
- (b) Normalization of the transcription signal to the cell area per depth image. This step alleviates the issues of cell size on transcription signal analysis. It showed reduction down to 0.67-fold of the original transcription signal without inhibition. Each dot is for single slice in ion tomograms.

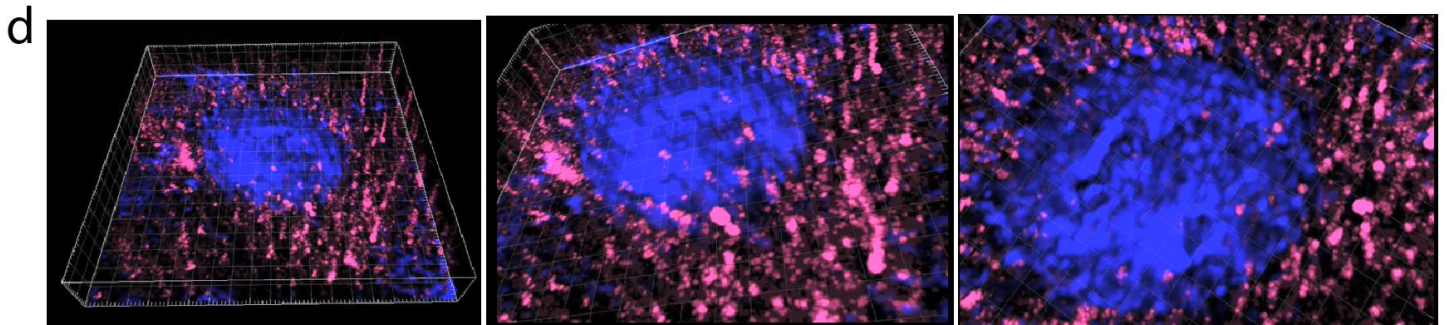
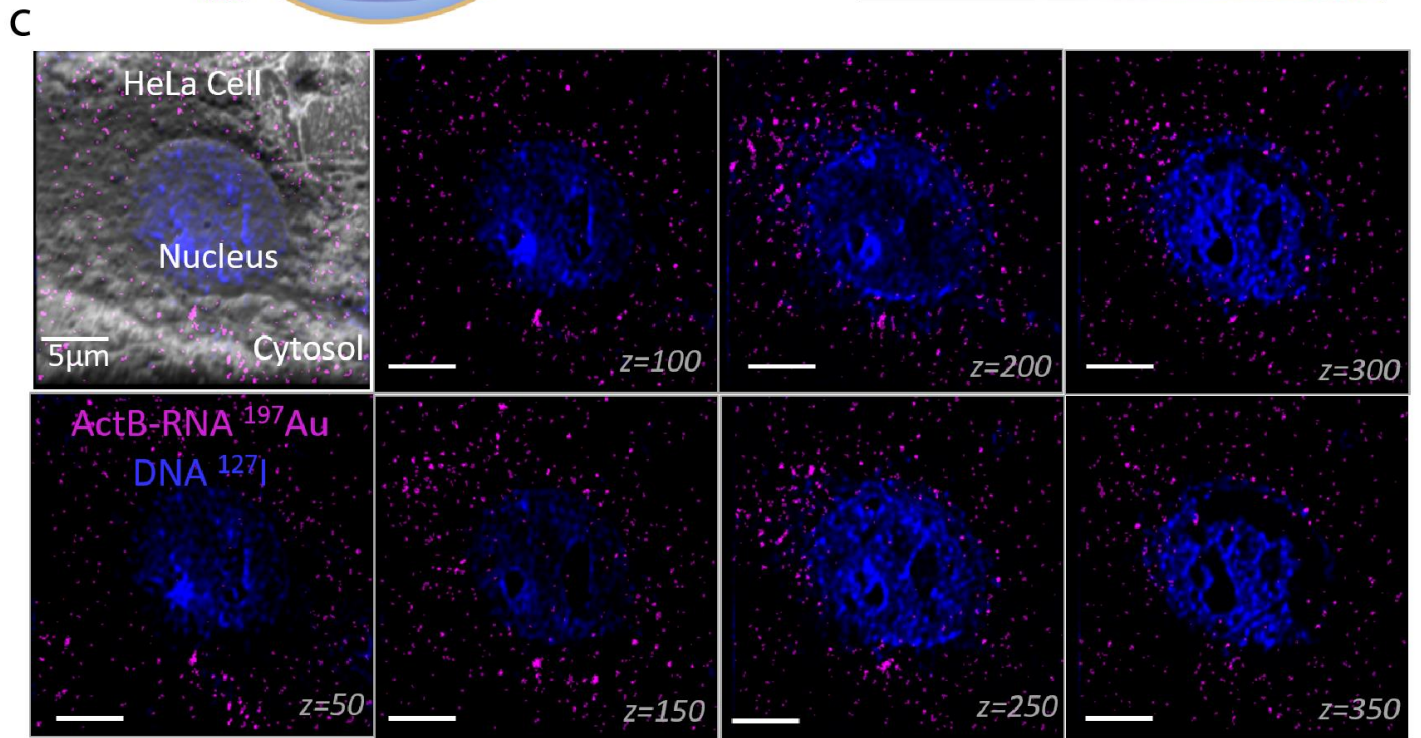
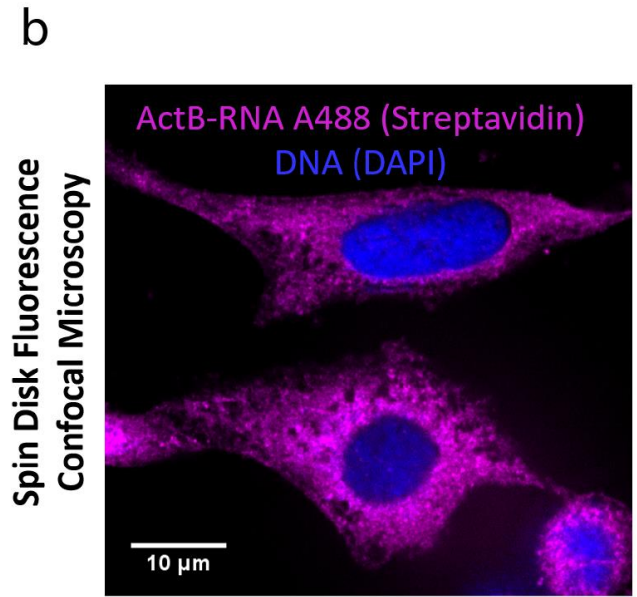
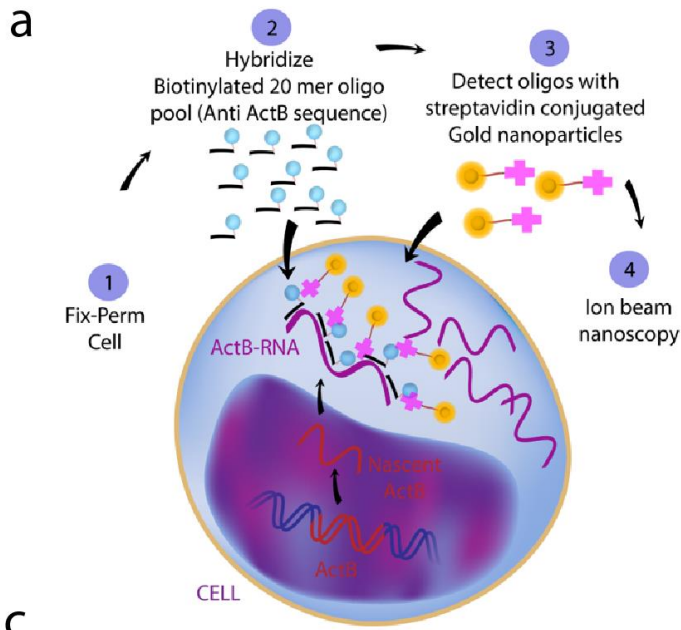


Supplementary Figure 32. IBT results do not depend on label. The experiment is the same as described in Supplementary Figure 18 except that transcripts were labeled with ^{127}I -rU and DNA was labeled with ^{81}Br -dU.

(a) Ion images for each row corresponds to a 50th, 75th, 150th, and 200th slices.

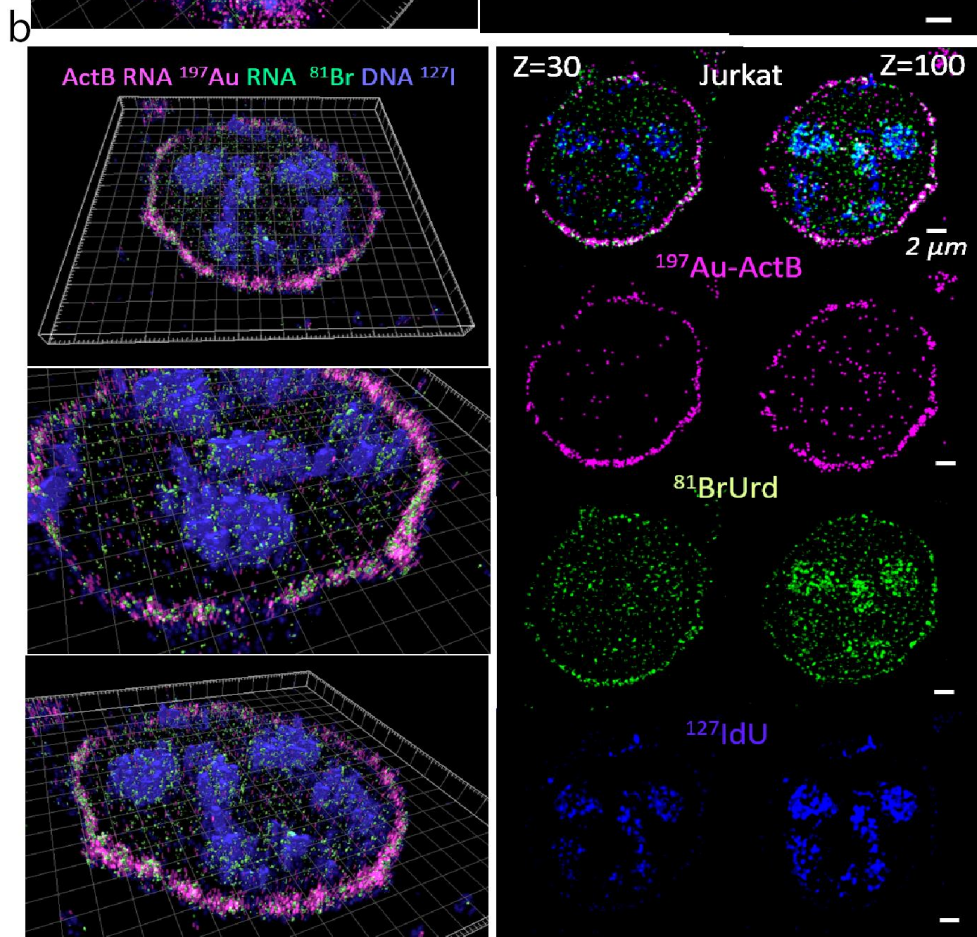
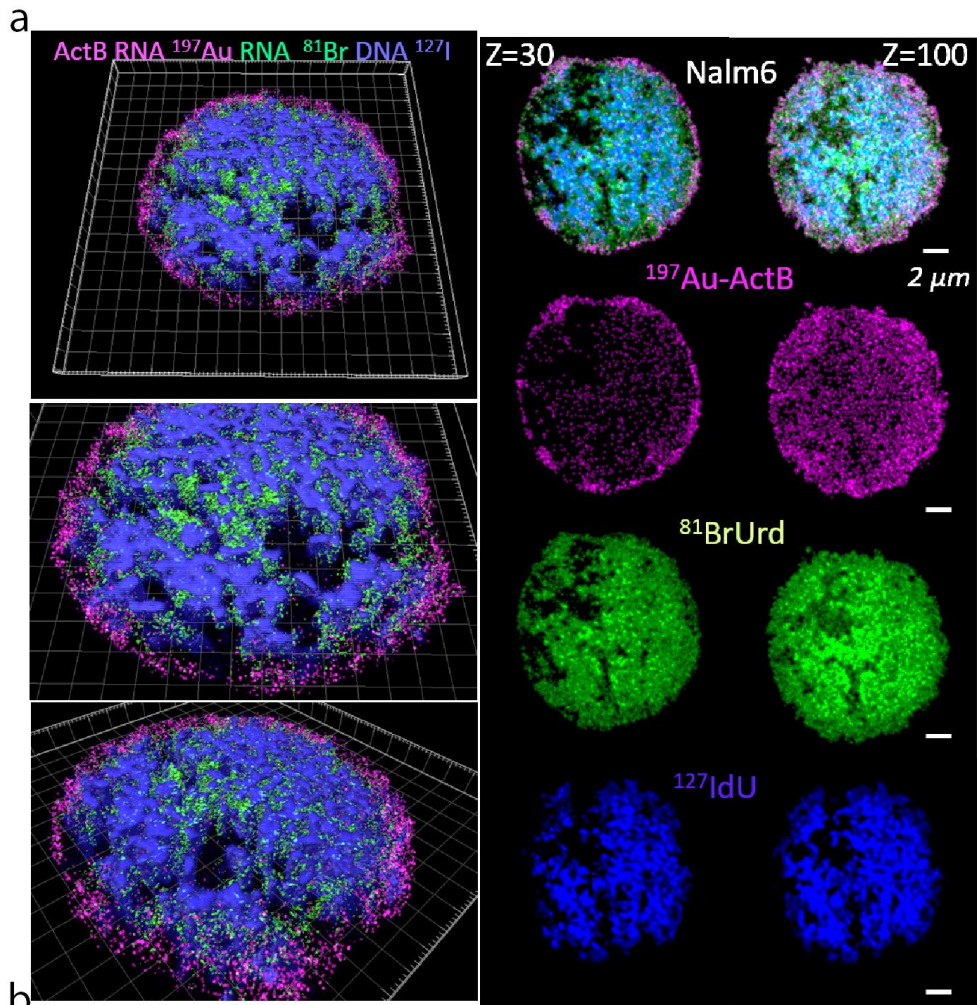
Note that these images were not processed by the mathematical pipeline, rather raw images were presented to describe spatial differences of individual pixels. 256x256 scans were used at 2 pA imaging current.

(b) Zoomed images from distinct slices (K, L, M, and N) showed non-overlapping pixels for newly synthesized transcripts and DNAs.



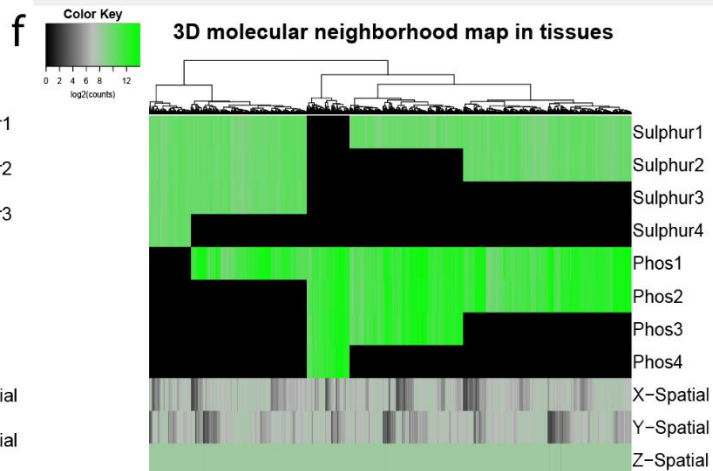
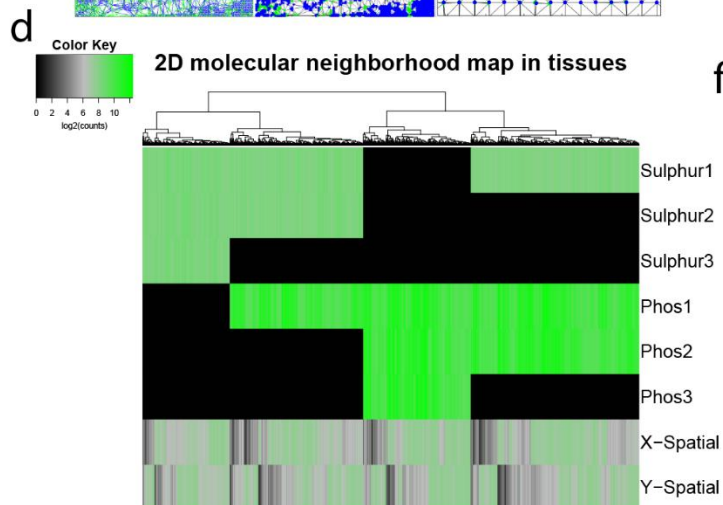
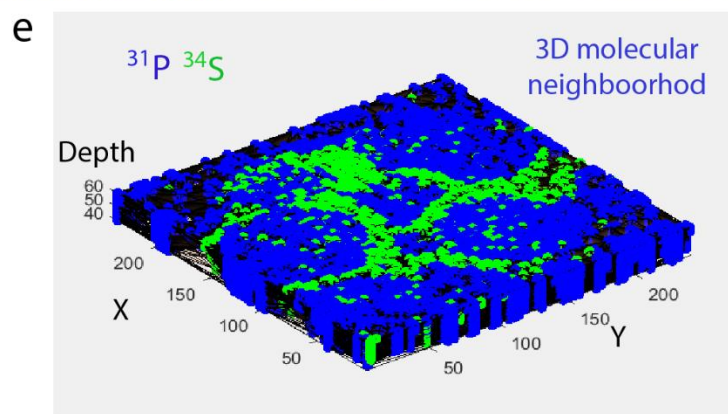
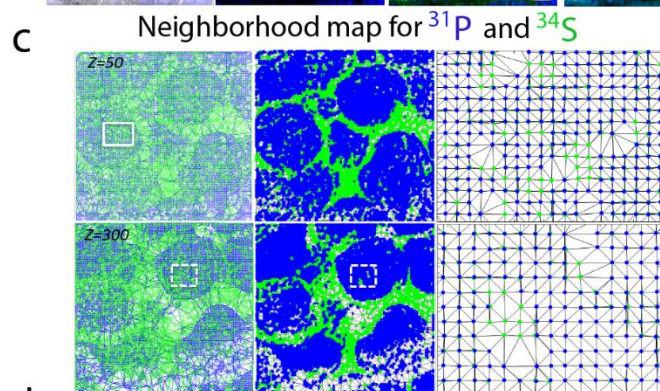
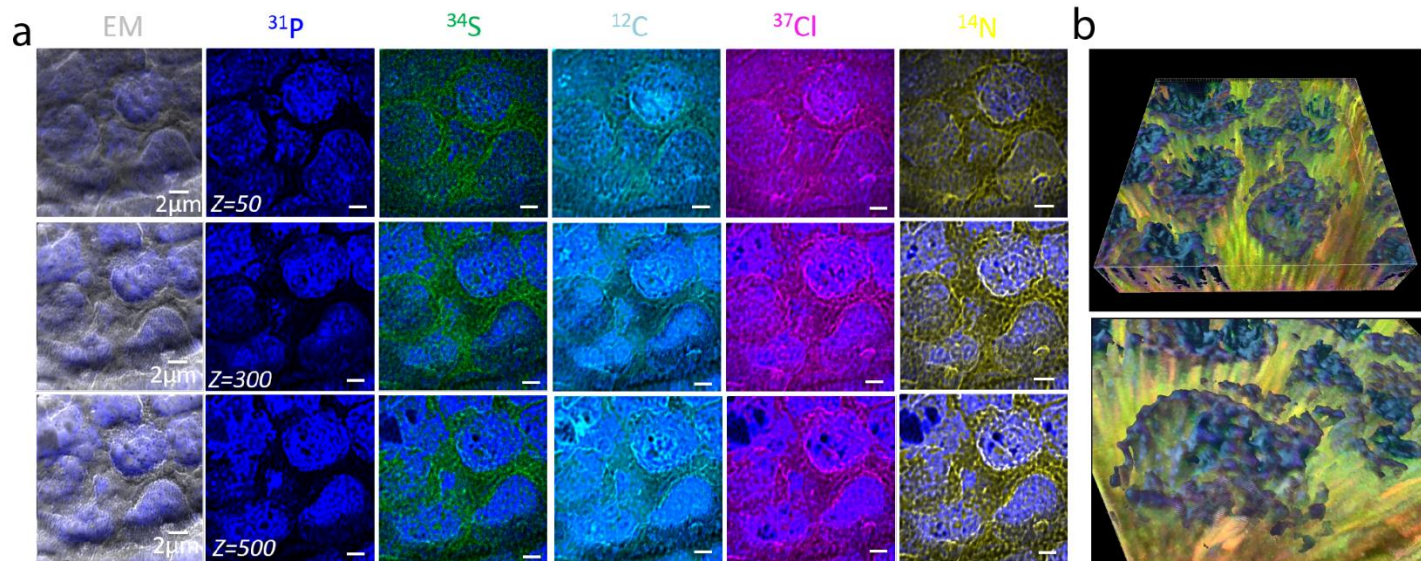
Supplementary Figure 33. Ion beam tomography maps transcriptional activity in individual HeLa cells.

- (a) RNA FISH was used to visualize *ActB* mRNA in a HeLa cell. After fixing and permeabilization of the cells, twenty-four biotinylated DNA probes designed to hybridize to the *ActB* mRNA were added to the cells. Streptavidin-conjugated gold nanoparticles were then incubated with the cells. Ion beam imaging was used to detect the probes in the ^{197}Au channel.
- (b) Using streptavidin-A488 secondary conjugates against oligonucleotides, we validated detection of *ActB* (magenta) in HeLa cells by spin disk fluorescence confocal microscopy. DAPI was used to visualize DNA (blue). Scale bar 10 μm . Most of these transcripts were mature, but we captured a few transcripts in nuclear regions.
- (c) IBT images of *ActB* mRNA in the 25- μm wide central part of a HeLa cell acquired across 450 slices. ^{127}I -dU (blue) was used to label DNA. Scale bars, 5 μm .
- (d) 3D renders of ion beam tomographic RNA images for *ActB* in a single HeLa cell from different viewing angles.



Supplementary Figure 34. Newly synthesized *ActB* transcripts and global transcription were measured together by ion beam tomography in Nalm6 and Jurkat cells.

(a and b) IBT images of DNA in the ^{127}I channel (blue, cells were labeled for with ^{127}I -dU for 23 hours prior to RNA labeling), newly synthesized RNAs in the ^{81}Br channel (green, labeled with ^{81}Br -rU for 1 hour after 1 hour of pulse), and *ActB* in the ^{197}Au channel (magenta, labeled with smFISH). The 30th and 100th slices are presented from each channel, demonstrating that *ActB* mRNA preferentially localizes at the periphery of both a) a Nalm6 cell and b) a Jurkat cell.

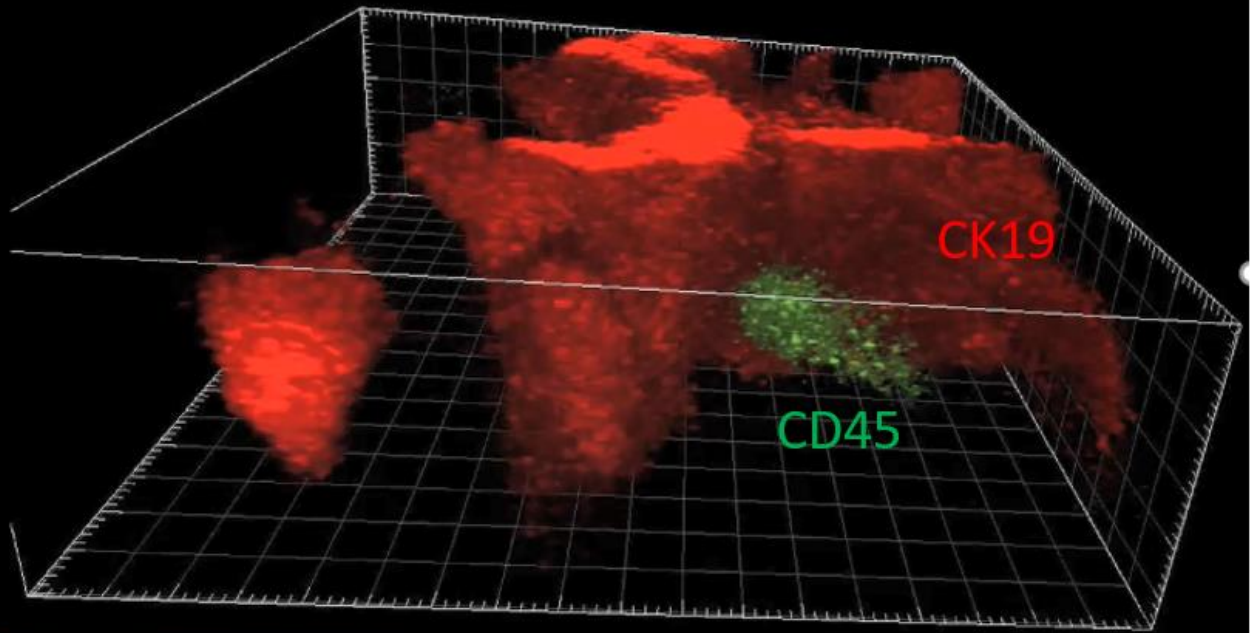
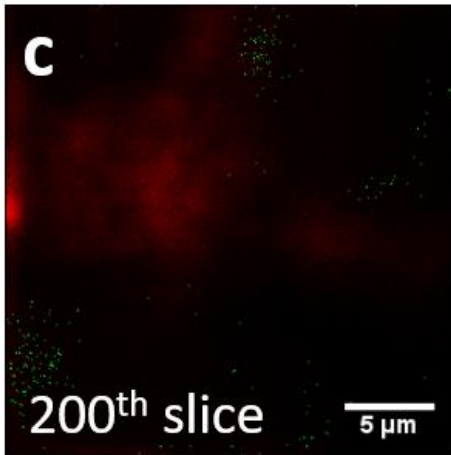


Supplementary Figure 35. Molecular neighborhood analysis of chromatin and proteins in FFPE tissues using IBT.

- (a) A label-free ion imaging panel for ^{31}P (primarily chromatin, blue), ^{34}S (proteins, green), ^{12}C (cyan), ^{37}Cl (red), and ^{14}N (yellow) in individual CD3^+ T cells from a lymph node biopsy core of a T cell lymphoblastic lymphoma patient. Sub-100-nm resolution images were acquired across 500 depth sections. Scale bars, 2 μm . Images in the first column show secondary total ion images as a bright field contrast of the cells. Each row is a 2D representation for 50th, 300th and 500th slices from ion tomograms.
- (b) IBT renders of single T cells with ^{31}P (blue), ^{34}S (green), and ^{37}Cl (red) co-localization resulting in yellow colors around chromatin islands.
- (c) Molecular neighborhood map of DNA (^{31}P) and protein (^{34}S) interactions in tissues. Two distinct depth images for 50th and 300th slices were processed by Delaunay triangles that were cornered with blue dots (^{31}P) or green dots (^{34}S).
- (d) Signals of each center-of-mass sub-regions were clustered by heatmap together with spatial positions (X-spatial and Y-spatial) of each triangle. Signals for ^{31}P were highly enriched in the nucleus, and other spatial sub-regions exhibit a combination of ^{31}P and ^{34}S signals. Delaunay triangles were cornered with a combination of phosphate (1-3) sulphur (2-3) signals.
- (e) 3D neighborhood analysis of twenty sections with Delaunay tetrahedrons that were cornered by four unique green (^{31}P) or magenta (^{34}S) dots.
- (f) Distinct neighborhoods were detected in the heatmap after clustering ^{31}P and ^{34}S with X-Y-Z spatial positions of tetrahedrons. Phosphate (1-4) and Sulphur (1-4) signals corner the tetrahedrons. Chromatin-protein interactions and protein-protein interactions exhibited spatial variations in different clusters.

a

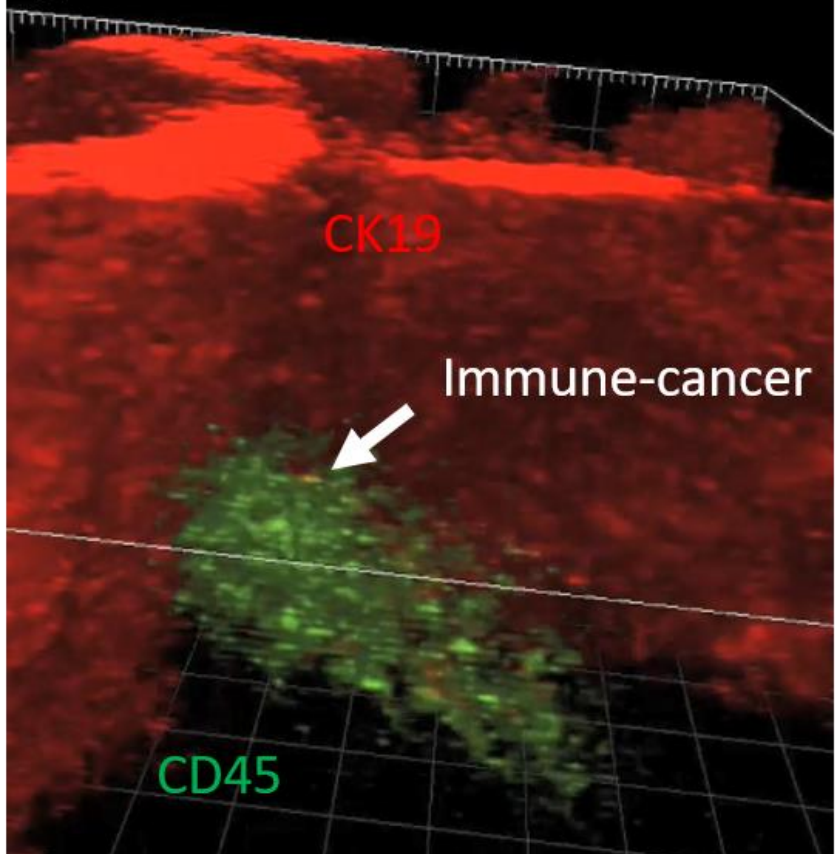
3D Immune-cancer imaging

**b**CD45 (^{169}Tm)CK19 (^{141}Pr)100th slice5 μm **c**200th slice5 μm **d**

CK19

Immune-cancer

CD45



Supplementary Figure 36. Volumetric histology by IBT.

(a) A sample of cholangiocellular carcinoma from a multi-tumor tissue microarray at 10- μm thickness was mounted on a silicon wafer for ion beam imaging by oxygen ion beam source.

(b) Immune cell (CD45⁺, label: ¹⁶⁹Tm) and cancer cells (CK19, label: ¹⁴¹Pr) were visualized.

(c) IBT collected at 420 depths allows digital focusing onto different layers (100th and 200th slices shown).

(d) 3D renders of connected cancer cells (red) and an immune cell (green).

Supplementary Methods

Tissues

Paraffin blocks of 70 unique different tissues were obtained from the archive of the Institute of Pathology, University of Bern, Switzerland. Cancer and normal tissue regions were annotated on corresponding hematoxylin and eosin stained sections. A tissue microarray of 70 cores measuring 0.6 mm in diameter was assembled using an automated tissue microarrayer (TMA Grand Master, 3D Histech). Prior to slicing, silicon substrates were treated with Vectabond (Vector Laboratories) to improve attachment of tissues on the surface. The tissue microarray block was then sliced onto the silicon substrates (18 mm x 18 mm) at 5-, 10-, and 15- μ m thickness. The final silicon samples with tissues were preserved in vacuum desiccator in the dark. To deparaffinize the tissue, the silicon substrate was manually treated sequentially with xylene (3 \times), 100% ethanol (2 \times), 95% ethanol (2 \times), 80% ethanol, 70% ethanol, and H₂O, each for 30 s. To perform antigen retrieval, the tissue was then placed in a plastic slide holder in target retrieval solution (Agilent, Dako) and loaded into a thermal cycler (PT Module, 97 °C for 40 min and cool down to 65 °C). After cooling to room temperature, the tissue was rinsed with a wash buffer (PBS 1 \times IHC with Tween 20 and 0.1% BSA). The sample then was dehydrated and directly imaged by IBT for label-free imaging of subcellular features (**Supplementary Fig. 35**).

Tissue staining

To enable labeling of mass reporters, after the antigen retrieval step, the tissue on silicon was treated with blocking buffer (TBS 1 \times IHC with Tween 20 and 3% donkey serum) for 1 h. After removing blocking buffer, the antibody mix (CD45⁺, label: ¹⁶⁹Tm and CK19, label: ¹⁴¹Pr) was loaded onto the sample and incubated overnight at 4 °C. The next day, the sample was rinsed with wash buffer and post-fixed with 2% glutaraldehyde (Electron Microscopy Sciences) for 5 min. After rinsing the sample with low barium PBS, the sample was washed with DI water and dehydrated for ion beam tomographic experiments (**Supplementary Fig. 36**).